Electrically-Tunable Near-Field Heat Transfer with Ferroelectric Materials

by

Yi Huang

Submitted to the Department of Mechanical Engineering
in partial fulfillment of the requirements for the degree of

Master of Science in Mechanical Engineering

at the

MASSACHUSETTS INSTITUTE OF TECHNOLOGY

June 2014

MASSACHUSETTS INSTITUTE OF TECHNOLOGY
AUG 15 2014
LIBRARIES
ARCHIVES

© Massachusetts Institute of Technology 2014. All rights reserved.

Signature redacted

Author .....
Department of Mechanical Engineering
May 3, 2014

Signature redacted

Certified by ....
Gang Chen
Carl Richard Soderberg Professor of Power Engineering
Thesis Supervisor

Signature redacted

Accepted by .....
David E. Hardt
Ralph E. and Eloise F. Cross Professor of Mechanical Engineering
Chairman, Department Graduate Committee

Electrically-Tunable Near-Field Heat Transfer with Ferroelectric Materials

by

Yi Huang

Submitted to the Department of Mechanical Engineering on May 23, 2014, in partial fulfillment of the requirements for the degree of Master of Science in Mechanical Engineering

Abstract

Radiative heat transfer at small separations can be enhanced by orders of magnitude via the use of surface phonon polariton or plasmon polariton waves. This enhancement has potential applications in different devices, such as thermal emitters, thermal rectifiers, thermophotovoltaic and thermoelectric energy conversion systems. In this thesis, the author explores the tunable optical properties of ferroelectric materials to manipulate the near-field radiative heat transfer between two surfaces, aiming at the active control of near-field radiation heat transfer. Soft mode hardening of ferroelectric thin films induced by environmental changes, such as temperature and electric field, is widely used as a basis for tunable and switchable electrical and optical devices. However, this mechanism has not yet been examined for heat transfer applications. Using the fluctuation-dissipation theorem and the Dyadic Green's function method, the author shows via simulation that the magnitude and spectral characteristics of radiative heat transfer can be tuned via an externally applied electric field and temperature. Ways are explored to maximize the tuning contrast and discuss the trade-off between maximizing tunablility and heat transfer. Our simulation results suggest that ferroelectrics can be used to develop new types of tunable nano-scale devices for thermal and energy conversion applications.

Thesis Supervisor: Gang Chen

Title: Carl Richard Soderberg Professor of Power Engineering

Dedication

To my loved ones.

Acknowledgements

I'd like to take the time to thank and appreciate the past two years I had at MIT. I enjoyed joining MIT and the Nanoengineering group under Professor Gang Chen, which is full of precious learning opportunities: discussions, presentations, seminars, etc. There were certainly also lots of difficult challenges in research and adjusting to graduate student lives, but now looking back, if not for these challenges, I'd not appreciate the hard-learned lessons. Exposure to the cutting-edge technologies, research, discussions at MIT have hinted me on how much I can still learn, explore and strive for better. My life goals and the possibility of reaching them never seemed clearer. Out of the influences I've had at MIT so far, the largest has to be the "people". It is those around us that make us better.

My advisor Professor Gang Chen gave me numerous supports and guidance in research. His personality, perseverance, and attitude towards research never fails to serve as a role model for me. Teammates who I work closely with in the "photonics" sub-group in the Nanoengineering Group: Dr. Svetlana Borsikina, Jonathan Tong, Poetro Sambegoro, Wei-Chun (Edi) Hsu, Dr. Selcuk Yerci. And of course many more who I enjoyed discussions with: Vazrik Chiloyan, Dr. Jivtesh Garg, Dr. Xiaopeng Huang, Bolin Liao, Jiawei Zhou, Geroge Ni, Jenny Wang, and the larger Nanoengineering Group. In the end, I'd also like to thank my fiancee Jiajun and my parents, without whose support I could never have made it through the past two years at MIT.

Contents

1 Introduction
1.1 Thermal Radiation
1.2 Motivations of Tunable Radiation Transfer
1.3 Current Methods of Tunability: Doped Silicon, Metamaterials, Graphene, Thermal Transistors
1.4 Proposed Mechanisms of Tunability
1.5 Thesis Outline

2 Near-Field Radiative Transfer
2.1 Maxwell Equations and Poynting Vector
2.2 Assumptions and Problem Formulation
2.3 Dielectric Materials and its Optical Properties
2.4 Surface Waves at the Interface: Surface Phonon Polaritons and Total Internal Reflection
2.5 Dyadic Green's Function for Parallel Half-Spaces
2.6 Fluctuation-Dissipation Theorem
2.7 Reaching Final Expression

3 Ferroelectrics
3.1 Phase Change and Temperature Dependence of Material Properties
3.2 Soft Mode Tunability with Temperature and Electric Field
3.3 Dielectric Response
3.4 Origins of Instability: Several Theories and Numerical Computations

4 Simulation Results
4.1 Dielectric Response of Ferroelectrics
4.2 Spectral Heat Transfer vs. Electric Field
4.3 Spectral Heat Transfer vs. Temperature
4.4 Transmission Function and Dispersion Relation
4.5 Total Heat Flux Tunability
4.6 Enhancement over Blackbody

5 Conclusions and Future Work
5.1 Other Control Mechanisms
5.2 What happens near phase transition?
5.3 Crystal lattice and Sub-wavelength control of Radiation
5.4 Outlook

Appendix A: Dyadic Green's Functions: Free Space as an Example
References

List of Figures

1.1 Experimental heat transfer coefficient between two silica materials, h vs. separation distance between them, d plotted with blackbody radiative heat transfer coefficient
2.1 Schematic of parallel half-bodies for radiative heat transfer
2.2 Lorentzian dielectric model without damping
2.3 Lorentz model with damping
2.4 Dispersion relation for bulk phonon polaritons of a Lorentz dielectric material without losses
2.5 Dispersion relation for Lorentz model with damping
2.6 Dispersion relation for bulk phonon polariton and surface phonon polaritons of a Lorentz material without losses
2.7: Parallel Half Spaces Configuration and Related Paramaeters
4.1: Fitted dielectric dispersion at T = 275K with experimental data from Kadlec et al. [56] plotted as data points
4.2 Top: Squared to frequency ω_{to}^2 vs. temperature for different electric fields; Middle: Uncoupled Debye response at various temperature; Bottom: Uncoupled Lorentz response at various temperatures
4.3 Typical dielectric response of ferroelectric material
4.4 Dielectric response with changing temperature and changing electric field
4.5 Spectral heat flux with changing electric field
4.6 Spectral heat flux with changing electric field
4.7 Spectral heat flux with changing temperature
4.8 Transmission function at 20k-80k configuration with 100nm separation
4.9 Total heat flux with changing electric field
4.10 Tunability of total heat flux at different temperatures
4.11 Enhancement of total heat flux over blackbody at different temperatures

List of Tables

4.1 List of Fitting Parameters for Dielectric Response
4.2 Values for Fitting Parameters for Dielectric Response

A.1 Green's function for different linear operators L

Chapter 1

Introduction

Control of heat flow has long been a pursuit for scientists and engineers. In this thesis, the author explores feasibility and methods to control thermal radiation. Due to high energy density of surface waves bound to the surface of a material, thermal radiation flux from one material to another can be greatly enhanced when the gap between them are on the nano to micro-scale. Nano to micro length scales are relevant to today's technology, and enhanced radiative flux can potentially be used in applications such as thermal transistors and rectifiers, thermophotovoltaics, thermal emitters, cooling of electronics and many more.

1 Thermal Radiation

Thermal radiation spectrum from a blackbody is usually described by Planck's theory of radiation [1] as

$$B_{\omega}(T)=\frac{\hbar\omega^3}{4\pi^3c^2}\frac{1}{e^{\hbar\omega/(k_BT)}-1} \tag{1.1}$$

Here T is temperature of the blackbody in thermal equilibrium, ω is angular frequency, $\hbar$ is reduced Planck's constant ($\hbar=1.055\times10^{-34}J\cdot s$), k_B is Boltzmann's constant ($k_B=1.381\times10^{-23}m^2\cdot kg\cdot s^{-2}\cdot K^{-1}$) and c is vacuum speed of light. The total amount of energy flux q depends on temperature of the blackbody T and is given by Stefan Boltzmann's law as $q(T)=\sigma T^4$, where σ is $5.670\times10^{-8}W\cdot m^{-2}\cdot K^{-4}$.

However, Planck noted in his original work [1] that Planck's law is the maximum radiative power from a material only when characteristic length, such as separation distance between two parallel planes, is large compared to the wavelengths of thermal radiation considered. Thermal radiation is fundamentally an electromagnetics problem, because atom vibrations inside the material induce oscillating electric charges that radiate as "antennas" to the surrounding. Therefore, when the characteristic length is comparable to the emission wavelength, wave-optics effects have to be considered. These effects include interference of electromagnetic waves and existence of evanescent waves. When characteristic length is larger than emitted wavelength, wave-optics effects can be ignored, and radiated power from blackbody is described by ray-optics and given by Planck's law.

At the interface between different materials, at least two types of evanescent waves can exist. One type comes from total internal reflection when waves emit from a positive high-refractive-index material to a low-refractive-index material at an angle larger than the

critical angle determined by Snell's law; such evanescent waves decay with distance only on the low-refractive-index side, but is propagating on the high-refractive-index side. Another type of evanescent wave is surface polariton wave, which comes from resonant coupling between photons and excitations within a material such as excitons and phonons. Surface polariton waves exist when the dielectric constants of materials on two sides of the interface have opposite signs. Surface polariton waves decay on both sides of the interface. Because both types of evanescent waves decay exponentially with distance away from surface of the material, thermal radiation depends on distance when characteristic length is smaller than decay length of evanescent waves.

To measure distance dependence of thermal radiation between two objects, one has to make sure separation distance is smaller than the dominant wavelength of emission. In 1960s, Domoto et al. measured heat transfer between copper thin disks at cryogenic temperatures [7] and showed that radiative flux increases as spacing between copper films decrease from 10^{-1} cm to 10^{-3} cm. Because the dominant wavelength of thermal emission is generally given by Wien's law $\lambda T = 3000 \mu m \bullet K$, at cryogenic temperatures, the dominant wavelength is on the order of millimeters and one can already observe via experiments distance-dependent thermal radiation at millimeter order spacing. The author notes that their goal was to explore how tunneling of evanescent waves that come from total internal reflection affect radiative heat transfer. Surface plasmon modes are not excited because plasmon frequencies are too high to be excited at cryogenic temperatures. However, due to low emissivity of metals, the total radiative heat flux is about 2% of the blackbody limit. Due to systematic measurement errors and other factors such as non-parallelism of copper disks, Domoto et al. made conservative conclusions that spacing indeed affect radiative flux, but suspected many experimental and modelling uncertainties exist. Several experiments were made to capture surface wave effects on thermal radiation [8,9] .These experiments all cumulated supporting evidence that surface wave effects cannot be ignored when characteristic length is smaller than dominant emission wavelength. In 2008 and 2009, Dr. Lu Hu and Dr. Sheng Shen, measured the amount of heat flux between hot and cold silica. Dr. Hu measured heat flux between two parallel plates and Dr. Shen measured heat flux between a sphere and a plate using a bi-material cantilever. The sphere-plane geometry can be approximated as plane-plane when the distance between a 100um-diameter sphere and plate are less than 1um. The author shows here their compiled measurement data of thermal heat transfer coefficient vs. distance d in Figure 1.1[2].

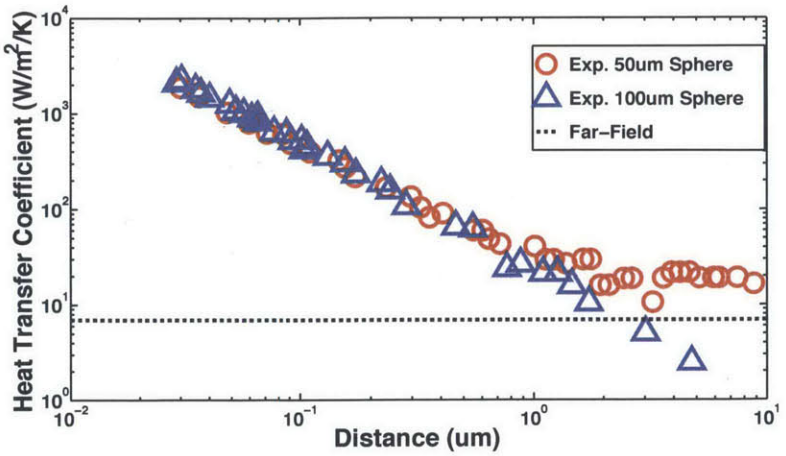

Figure 1.1: Experimental heat transfer coefficient between two silica materials, h vs. separation distance between them, d plotted with blackbody radiative heat transfer coefficient

The measured heat transfer coefficients of radiation between two silica materials at room temperatures are shown in Figure 1.1 as a function of distance [2]. The blackbody radiative heat transfer coefficient is denoted by the horizontal line and can be approximated for T_1 =332.15K and T_2 = 293.15K. Then the heat transfer coefficient h can be given as $h=\sigma(T_1^4-T_2^4)/(T_1-T_2)\approx 4\sigma(\frac{T_1+T_2}{2})^3=6.93 W/m^2/K$. The figure also shows that radiative heat transfer is independent of the separation d between hot and cold sides, which agrees with Stefan-Boltzmann's law. Figure 1.1 clearly shows that radiation heat transfer coefficient depends on separation d between two materials. For distance d greater 10um, heat transfer coefficient h is asymptotic to the far-field value. As distance d becomes smaller than the decay length of evanescent surface wave, h increases. Recent literature often refers to the regime when surface waves contribute to radiation heat flux as the 'near-field' regime. Blackbody radiation is often referred to as 'far-field radiation' as when surface wave effects don't play a significant role.

Near-field radiative heat transfer has become more and more relevant in micro and nano scale devices in the last decades. Previously, radiation is generally neglected in many heat-transfer problems except at elevated temperatures and when surface area of object is large. However, length scales of materials and devices began to drop significantly to the 'near-field' regime, due to advances in micro-nano technology, and even at room temperatures, the amount of heat transfer cannot be neglected. For example, modern technologies make disk drives with a typical gap of 3nm. It is clearly in the 'near-field' regime. In addition, advanced manufacturing techniques can exploit the large heat flux in near-field regime to create devices, such as thermophotovoltaics[12].

2 Motivations of Tunable Radiation

Controlling how carriers transport has been extremely useful in the history of technology development. For instance, electron transport is controlled in transistors to represent logical operations. Research has also been conducted to build optical transistors for optical communications. Because there exist numerous applications for controllable transport phenomena, it is of both scientific and technological interest to investigate ways to control radiative heat transfer.

Thermal radiation depends strongly on a few parameters. Because lattice vibrations is the source of thermal radiation, changing lattice properties of the material changes its thermal radiative properties. In addition, because transport phenomena rely heavily on what happens at the interface, surface properties of the material also change radiation properties. Density of optical states within the material can also be changed to modify near-field radiative transfer by changing thickness and geometry of the material. All these properties of thermal radiation give researchers versatility in controlling radiation transport. This thesis will rely heavily on the above properties to achieve the goal of controlling radiation transport.

Active control of radiation transfer by an external factor, such as electric field and laser light, is desirable. Since electric field is one of the most convenient methods for active control, the author explores in this thesis electric-field tuning of radiative transfer. In order to motivate study of tunable near-field heat transfer, the author explains in the following few paragraphs several proposed applications using near-field effects of radiation, and how tuning can aid these applications.

The author notes that although the thesis mainly explores tunable heat transfer in the near-field regime, changing near-field radiation properties also change far-field radiation properties.

One proposed use of the high-energy surface waves in the vicinity of a material is thermal emission [15] Although thermal emitters radiate in the far-field, changing near-field radiation of a thermal emitter also modifies its far-field characteristics. Greffet et al. added gratings on top of silicon carbide to create the first thermal emitter which couple the phonon polariton modes normally existing at the surface to above the light line [15].

Due to nature of a emitter, it is desirable to actively tune its emission properties, such as radiation patterns and coherence. Hafeli et al. [72] put a grating structure on top of α-SiO2 and showed that the far-field reflection characteristics of the sample change with temperature because the dominant wavelength of emission changes, and emitted photons interacts differently with the grating structure. However, the grating structure is fixed and cannot be tuned by external factors. It is desirable to show that the far-field characteristics of a thermal emitter changes just by applying electric field.

It was also proposed that enhanced radiation flux in near-field regime can be used for thermophotovoltaics (TPV) cell. TPV cells were first explored in the late 1950s[13] and usually comprises of a solar absorber, thermal emitter to emit thermal radiation and a typical p-n junction to convert re-emitted photons to electricity. TPV's potential to harvest electricity from thermal

emitters has been demonstrated experimentally by researchers in the last few decades[10, 11, 12] with highest efficiency of 3-5%[12]. All work performed on TPV cells is in the far-field regime with a gap distance greater than 100μm, but the enhanced near-field heat flux can increase the power output from the device significantly. Several proposed emitter-receiver configurations include: graphene-covered hexagonal Boron Nitride emitter with a p-n junction receiver [24] and photonic crystal emitter with silicon PV cell receiver[20].

However, a drawback for TPV cells is the mismatch in frequency of the thermal emitter and the photovoltaic receiver, and tunable radiative heat transfer devices can potentially aid in matching the frequency of the emitter to that of the receiver, increasing efficiency of the TPV cell. This is because photovoltaics operate most efficiently at energies greater than a certain bandgap, but thermal emitters have broadband emission spectrums.

Cooling of electronics is another proposed application for enhanced near-field radiative heat flux. Experiments have shown a 1.5K drop in electronic or surface temperature, by simply bringing a glass probe close to the surface [26]. Heat extractors are also built by enclosing a black surface using a hemispherical dome, which acts as a cavity resonator and increases the density of optical states for the field the black surface emits into. These heat extractors demonstrate far-field extraction of radiation [14] and may be used for radiative cooling of surfaces. Electric-field control of near-field heat transfer adds another dimensionality in controlling cooling of electronics on chip. For example, one can turn "on" or turn "off" the areas one intends to cool simply by applying an electric field. Fabrication techniques for ferroelectrics is also well-developed because ferroelectrics is used in memory systems called FeRam. However, the author doubts the practicality of the application since experimental demonstrations showed a mere 1.5K drop in temperature so far.

3 Current Methods of Tunability: Doped Silicon, Metamaterials, Graphene, Thermal Transistors

Graphene, doped silicon and metamaterials are the most widely explored materials for tunable thermal transport. Tunability largely depends on the tunable properties of the material. It is also tunability of ferroelectric materials that this work relies on.

Doped silicon shows surface phonon polariton modes in the infrared primarily due to interaction of light with free carriers. Since the amount of doping changes the amount of free carriers inside silicon, the dielectric response of doped silicon changes with doping concentration. A few research groups have shown via calculation that [27] by changing the amount of dopant concentration by 2-5 orders of magnitude, heat transfer increases as much as 100% at gap distance around 100nm. However, dopant concentration in semiconductors is fixed and gating the material usually cannot alter the dopant concentration by a few orders of magnitude, at least not for lightly doped materials. One may also use light to generate additional free carriers inside semiconductors, which in turn adds conductivity to the material and change its optical properties. Such effects have been both experimentally and theoretically explored by researchers in the

The proposed mechanisms in the graphene case also explores the effect of coupling strength between opposing materials on the total heat flux. In general, the more different the opposing materials, farther apart their resonance frequencies, and thus less coupling occurs, and less heat is transferred.

A recent mechanism was proposed by Ben-Abdallah et al. [35] for thermal transistors. Instead of the usual configuration of one hot plate facing one cold plate, the paper suggests sandwiching a third material between hot and cold plates. The material in between is a phase-change material, such as vanadium oxide. Above phase change temperature,vanadium oxide is reflective, while below the phase change temperature, it is absorbing. This property of vanadium oxide allows it to act as a "gating" material between hot and cold side, and can in turn be controlled externally via another heat system. The author shows that by changing temperature of vanadium oxide in the middle, one can switch the heat flux between two materials on and off.

4 Proposed Mechanisms of Tunability

In this thesis, we explore two mechanisms on which tunability of heat transfer relies on, namely

- Material property changes with temperature and electric field
- Opposing materials with different surface wave modes

Because ferroelectrics material is a phase-change material, its dielectric properties change as the temperature and electric fields are varied. Using electric field, dielectric constant of certain ferroelectrics shift by close to 1THz in the infrared frequency spectrum. As temperature changes, dielectric constant of ferroelectrics can shift on the order of 10THz. Changes in dielectric response of the material also shifts frequency of surface phonon polaritons ω_{SPP}. As mentioned previously, surface polariton waves contribute significantly to radiative heat transfer, so changing frequency of these surface waves alter the radiation characteristics.

The second mechanism depends on how well modes on hot and cold sides couple with each other. If modes are at the same frequency, coupling is strong; vice versa, the coupling is weak. Suppose that one side of the structure supports surface phonon polaritons at frequency ω_{SPP}^{H}, and the other side supports it at $\omega_{SPP}^{C} \neq \omega_{SPP}^{H}$. Due to the frequency difference, surface phonon polaritons cannot couple strongly across the interface, and thus less energy is transferred.

In addition, due to the statistical nature of thermal radiation, different frequencies of modes are excited at different temperatures. Depending on modes of transport across the gap, temperature can also change the spectrum of heat flux significantly.

5 Thesis Outline

The remaining thesis will be divided into 4 main parts. The first two parts will lay theoretical foundations of two components within our model: near-field thermal radiation and ferroelectrics.

Casimir force community[28,29] to show an optical modulation of Casimir force between silicon membranes.

Fu et al. [27] calculated how radiative heat flux changes for different doping levels of silicon at separation distances 1nm – 10um. At 100nm separation distance, radiative heat transfer between silicon half-bodies does not change significantly when doping level increases to 10^{18} cm^{-3}. It is only at around 50nm, the change is evident. A more promising result [32]shows a larger contrast in heat transfer coefficient for p-doped silicon. With a change in doping from $3.09\times10^{19}cm^{-3}$ to $2.03\times10^{20}cm^{-3}$, the conductance dropped half from 4 nW/K to below 2 nW/K at 100nm separation. J. W. Shi et al. also performed experiments which showed considerable agreement to the simulations. However, to achieve such large change in doping can prove to be experimentally challenging. Authors of the above paper have not indicated any active mechanism to change semiconductor doping that can be used for tunable near-field heat transfer.

Meta-materials can also show negative permittivity at certain frequencies. As discussed in Section 1.2, materials with negative permittivity when interfacing with vacuum are able to sustain surface polariton waves, which greatly enhance radiative heat transfer. For the purpose of thesis organization, details of the effects of surface phonon polariton waves are included in Chapter 2 .

Metamaterials are usually made up of repeating patterns of elements such as split-ring resonator and dielectric rods. By changing the properties of its constituent materials, surface polariton modes also changes, which in turn changes radiative transfer. Conventional ways of changing optical properties of metamaterial involve using phase change materials, ferroelectrics and ferromagnetics, light modulation or bimaterial cantilevers to mechanically actuate split-ring resonators. Calculations by Cui et al. [33] showed that tunable magneto-electric coupling in chiral metamaterials is also useful for tunable radiative heat transfer. In a chiral metamaterial, electric field induces magnetic polarizations and magnetic field induces electric polarizations. Chirality strength Ω_K, which indicates strengh of magneto-electric coupling, is one of the determining factors for the frequency of surface polariton mode. Changing chirality strengths of opposing materials Ω_{K_1} and Ω_{K_2} significantly shifts the frequency of polariton modes supported. For example, in Cui's paper[33], the authors showed a shift in spectral heat flux of $0.1\omega_0$, where ω_0 is the dielectric, magnetic and chirality resonance of the metamaterial.

Graphene was explored by Ilic et al. in 2010 [34] as a candidate for tunable thermal radiation. Dielectric dispersion of graphene shows surface plasmon modes in near-infrared, and can be changed by a large amount via gating or doping. The authors calculated a large frequency shift in spectral heat flux due to the large shift in plasmon frequency in graphene. Gating is a well-explored technique and could be easy to implement experimentally. However, the authors do not argue for a large total heat flux change and do not show how much the absolute change in heat flux is.

Chapter 2 will first describe Maxwell equation and general treatment of energy transport using waves, surface waves, fluctuation dissipation theorem which describes generation of electron fluctuations due to atomic vibrations and Green's function which describes response of the surroundings due to source currents. Chapter 2 will conclude with a detailed derivation that leads to the final formulation of equations.

Chapter 3 will introduce the reader to basic concepts of ferroelectrics and why the author is interested in using ferroelectrics for near-field radiation applications. The chapter begins by looking at phase change and the abnormally large dielectric response at phase transition temperature. Microscopic descriptions of optical properties of dielectrics are also introduced. The author will then discuss origins of tunable crystal structure inside ferroelectrics in two perspectives: total free energy and the atomic picture, followed by a brief discussion of related theories.

Chapter 4 will show the main results of our current simulation models. Three results demonstrate tunability of radiative heat transfer: (1) electric-field control of spectral heat transfer; (2) temperature control of spectral heat transfer; (3) control of total heat transfer. In each section, the author goes into details of why such tenability occur and why it is more prominent at some conditions more than other. Other supporting sections will describe enhancement of heat flux over blackbody and many more.

The author concludes in chapter 5 with a summary of current work and look into possible extensions of current work in the future. Future work will be divided into 3 parts: (1) use of other ferroelectric materials to push up tunability; (2) other control mechanisms to control near-field heat transfer that rely less heavily on material properties; (3) control of surface phonon polariton properties by changing phonon transport in the lattice using defects for example.

Chapter 2

Near-Field Radiative Transfer

The primary mode of radiative heat transfer is photon transport. Photons are generated in the dielectric material by electron fluctuations that act like antennas. Atoms vibrate, causing electrons surrounding the atoms to vibrate; vibrating electrons and atoms act like oscillating dipoles, which in turn emit radiations. Figure 2.1 shows the schematic of the radiation problem looked at in this thesis: two parallel semi-infinite materials separated by a gap *d*.

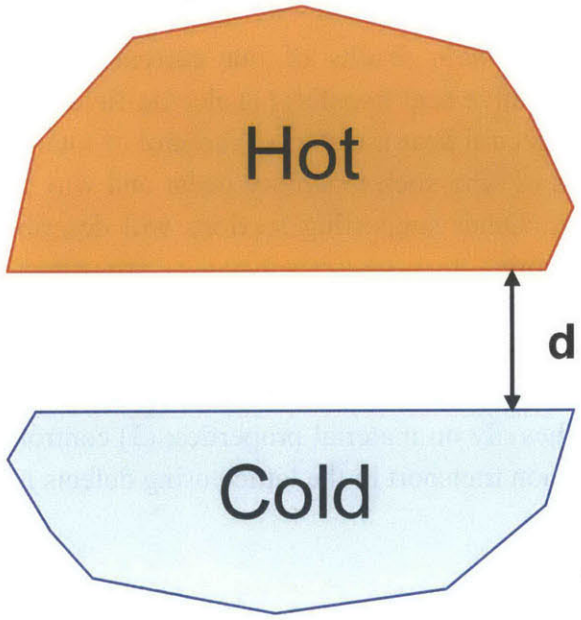

Figure 2.1: Schematic of Parallel Half-Bodies for Radiative Heat Transfer

Semi-infinite materials contain an infinite amount of dipoles oriented randomly inside that dissipate energy in the form of electromagnetic waves. How radiation is generated from electron fluctuations inside the material can in turn be described via dielectric constant. Dielectric constant is the material response to external dielectric field; vice versa, it also describes excitation of external electric field from electric fluctuations inside the material itself. Dielectric constant relates to the material's response function due to a perturbation that can be both external and internal to the material.

Since the primary carrier of energy is photon, Maxwell equations are used as the basis of near-field radiative transfer calculations. Maxwell equations tell us how materials respond to charges, current, external electric field and magnetic field. Green's function, which describes the

solution of Maxwell equations for different geometries, is used in the this thesis. Although Green's functions have different forms from Maxwell equations, Green's function describe the same physics as Maxwell equations. The author notes that Dyadic Green's function (DGF) is just the tensor-form of scalar Green's function.

To relate back to sources of photons and radiation, fluctuation-dissipation theorem (FDT)[5, 36] is used to describe how electron fluctuations are generated by thermal excitations. Combining Maxwell equations (or Dyadic Green's functions in this thesis) and fluctuation-dissipation theorem, the amount of energy carried by thermally-excited photons can be calculated. The first complete derivations for near-field radiative flux is given by D. Polder et al.[4], where he used Maxwell equations and fluctuation dissipation theorem. The following derivations for near-field radiative heat flux is formulated after several papers [6, 17, 19] using Dyadic Green's function and Fluctuation Dissipation Theorem.

1 Maxwell Equations and Poynting Vector

Maxwell equations are four equations as listed below. They describe relations between electric displacement $\vec{D}$, electric field $\vec{E}$, magnetic displacement $\vec{B}$, magnetic field $\vec{H}$, current $\vec{J}$ and density of free charges ϱ.

$$\nabla \cdot \vec{B} = 0$$
$$\nabla \cdot \vec{D} = \rho$$
$$\nabla \times \vec{E} = -\frac{\partial \vec{B}}{\partial t}$$
$$\nabla \times \vec{H} = \frac{\partial \vec{D}}{\partial t} + \vec{J} \qquad (2.1 - 2.4)$$

The electric displacement and electric field are related by dielectric constant or permittivity ε, while magnetic displacement and magnetic field are related by magnetic permittivity μ. Vacuum electric and magnetic permittivity are ε_0 and μ_0 respectively. The relative dielectric constant are unit less and is the ratio between the material permittivity and the vacuum permittivity. In all following sections, ε and μ denote relative dielectric constant and relative magnetic permittivity respectively.

$$\nabla \vec{D} = \epsilon \epsilon_0 \vec{E}$$
$$\nabla \vec{B} = \mu \mu_0 \vec{H}$$
$$\frac{1}{\epsilon_0 \mu_0} = c_0^2 \qquad (2.5 - 2.7)$$

In order to relate Maxwell equations to energy flow or heat flux, poynting vectors are introduced. Poynting vectors are defined as energy flow across per unit area and is described by

$$\vec{S} = \vec{E} \times \vec{H} \qquad (2.8)$$

Since poynting vector is defined microscopically at a time instant and at a specific point, it is not easily measured physically. To relate to physical identities, a time-average is taken assuming all fields are time-harmonic fields:

$$\begin{aligned}\vec{S} &= \vec{E} \times \vec{H} \\ &= Re(\vec{E}_c e_{i\omega t}) \times Re(\vec{H}_c e_{i\omega t}) \\ &= \frac{1}{2}(\vec{E}_c e_{i\omega t}) + \vec{E}_c^{\,*} e_{-i\omega t}) \times \frac{1}{2}(\vec{H}_c e_{i\omega t} + \vec{H}_c^{\,*} e_{-i\omega t}) \\ &= \frac{1}{2} Re(\vec{E}_c \times \vec{H}_c^{*}) + \frac{1}{2} Re(\vec{E}_c \times \vec{H}_c^{*} e^{2i\omega t})\end{aligned} \tag{2.9}$$

Therefore the time averaged energy flow is $\frac{1}{2}Re(\vec{E} \times \vec{H})$, which will be used in the following derivations.

2 Assumptions and Problem Formulation

Assume that relative magnetic permittivity μ is 1, and homogenous across the entire geometry which include both parallel half-spaces and the medium in between. Also assume that ω is non-zero. By Fourier transform one can always decompose the field into summation of time-harmonic fields for different frequencies, so it is justified to assume that for a specific frequency, field can be described by $e^{i\omega t}$.

To look at a simpler problem first, suppose there is no free charge and no current. Then Maxwell equations can be described as an eigenvalue problem by taking the curl of Eq. 2.1. Plugging in Eq. 2.4, Eq. 2.10 below reads

$$\begin{aligned}\nabla \times \nabla \times \vec{E} &= -\nabla \times \frac{\partial \vec{B}}{\partial t} \\ &= -\nabla \times i\omega\mu_0\mu\vec{H} \\ &= -i\omega\mu\mu_0(\nabla \times \vec{H}) \\ &= \frac{\omega^2}{c_0^2}\epsilon\mu\vec{E}\end{aligned} \tag{2.10}$$

Left-part of the equation can be viewed as an operator. Under the divergence equations Eq. (2.1) and Eq. (2.2), as well as boundary conditions such as $\vec{E} \times \vec{n} = 0$ (TM polarization), Maxwell equations become a general eigenproblem., where $\nabla \times \nabla \times$ and $\varepsilon(\vec{r})$ are both operators on $\vec{E}$.

Green's function can then be used to solve for the response function of the system. Green's function is the integral kernel for an inhomogeneous differential equation. In the scope of this thesis, an inhomogenous Helmholtz equation, as will be shown later, is solved. Suppose the inhomogeneous differential equation is $\hat{L}F(x)=f(x)$, where $\hat{L}$ is a linear operator, and $G(x,\alpha)$ satisfies $\hat{L}G(x,\alpha)=\delta(x-\alpha)$ at certain boundary conditions. Then solution of the inhomogenous differential equation $F(x)= \int G(x,\alpha)f(x)dx$ is the convolution of f(x) and the Green's function $G(x,\alpha)$.

The proof is straightforward. Given $\hat{L}G(x,\alpha)=\delta(x-\alpha)$, and that operator $\hat{L}$ is entirely linear on variable x, then

$$
\begin{aligned}
f(x) &= \int \hat{L}G(x,\alpha)f(\alpha)d\alpha \\
&= \int \delta(x-\alpha)f(\alpha)d\alpha \\
&= \hat{L}u(x) \\
&= \hat{L}(\int G(x,\alpha)f(\alpha)d\alpha)
\end{aligned}
$$

Therefore,

$$u(x)= \int G(x,\alpha)f(\alpha)d\alpha \tag{2.11}$$

Using the conventions above, we define the Green's function for electric field as the solution to Eq. (2.12)

$$\nabla \times \nabla \times \vec{E} - \frac{\omega^2}{c_0^2}\epsilon(\vec{r})\mu\vec{E} = \delta(\vec{r}-\vec{r}') \tag{2.12}$$

Suppose now that there exists current $\vec{J}$ as well, which in the problem described here, comes from thermally excited electron fluctuations. One can obtain Eq. (2.13) instead of Eq. (2.10):

$$\nabla \times \nabla \times \vec{E} - \frac{\omega^2}{c_0^2}\epsilon\mu\vec{E} = -i\omega\mu\vec{J} \tag{2.13}$$

By vector identity $\nabla \times \nabla \times \vec{E} = \nabla(\nabla \cdot \vec{E}) - \nabla^2\vec{E}$, $\nabla \cdot \vec{E} = 0$ from Maxwell equations, and $\frac{\omega}{c_0} = k$, Eq. (2.13) can be rewritten as

$$\nabla^2\vec{E} + k^2\epsilon\mu\vec{E} = i\omega\mu\vec{J} \tag{2.14}$$

Therefore, in terms of Green's functions defined as the solution of Eq. (2.12), the electric field can then be written as

$$\vec{E}(\vec{r},\omega) = i\omega\mu \int_V dV'\bar{\bar{G}}_E(\vec{r},\vec{r}',\omega)\cdot\vec{J}(\vec{r}',\omega) \tag{2.15}$$

where $\vec{r}\,'$ denotes the source terms, and $\vec{r}$ is the position of the field. In the following paragraphs, the author solves the Green's function as an impulse response function to the inhomogenous differental equation Eq. (2.12).

One should note that Green's function can be solved **without** adding current $\vec{J}$, although current is treated as the source of radiation in our electromagnetics formulation. In a system where electric current J can be completely described in relation to the electromagnetic field, one can use Ohm's law or Boltzmann Transport Equation to relate current $\vec{J}$ to electric field $\vec{E}$ by $\vec{J} = \sigma\vec{E}$ or $\vec{J} = -en\vec{v}$ where σ is conductivity of the material and $\vec{v}$ is the mean velocity of free carriers. One then obtains $\nabla \times \nabla \times \vec{E} = (\frac{\omega^2}{c_0^2}\mu\epsilon(\vec{r}) - i\omega\mu\sigma(\vec{r}))\vec{E}$ and can solve it as an eigenproblem

as well. However, in our current formalism where $\vec{J}$ is thermally excited, it is not possible to describe $\vec{J}$ by $\vec{J} = \sigma\vec{E}$.

However, solving the above inhomogeneous equations is non-trivial in complex geometries and for complex materials. Mathematicians and physicists developed systematic ways to solve for Green's functions.

The magnetic field can also be related to Green's function as below.

$$\vec{H}(\vec{r},\omega) = \int_V dV' \bar{\bar{G}}_H(\vec{r},\vec{r}',\omega) \cdot \vec{J}(\vec{r}',\omega) \tag{2.16}$$

As in Maxwell equations, the Green's functions of magnetic and electric field G_H and G_E is also related as

$$G_H = \nabla \times G_E \tag{2.17}$$

because $\nabla \times \vec{E} = i\omega\mu H$ and that the magnetic field also satisfies the inhomogenous Helmholtz equation. One can find detailed derivations using symmetric Maxwell equations described by Narayanaswamy et al.[18]. This relation can be used to simplify our calculation. The average Poynting vector defined as in Eq. 2.9 is equal to $\vec{S}(\vec{r},\omega) = 4 \cdot \frac{1}{2}\vec{E} \times \vec{H}$ where the factor of 4 is because in Fourier decomposition of time-dependent fields, only positive frequencies are considered.

3 Dielectric Materials and its Optical Properties

Describing optical properties of dielectric materials are crucial for understanding physical origins of surface phonon polaritons and thus enhanced near-field radiation. So this section will focus on describing useful formulations and ways of thinking when dealing with dielectrics.

Most dielectric materials can be described by the Lorentz model, while metals can be described by Drude model. Both models were first derived using classical physics, and later extended using quantum mechanics. To understand Lorentz model, one has to first describe polarization $\vec{P}$ of the material, or how much dipole moment is induced by an external electric field. The following derivations is primarily based on Ashcroft and Mermin[40]. Microscopically, there are two contributions to the dipole moments induced in the material: (1) atomic polarizability, which describes dipole moment induced in a single atom by displacement of the electron cloud from its nucleus; (2) dipole moment induced from relative displacement of ions.

Atomic polarizability can be described by an electron cloud shell connected to the nucleus of the atom by a spring. The induced dipole moment can be described by $\vec{p} = -Ze\vec{r}$, where Z is the electron number, e is the charge of an electron, and r is the displacement of the electron cloud from the nucleus. Ignoring damping and assuming an external electric field, the equation of motion for the electron cloud is given as:

$$Zm\frac{d^2r}{dt^2} = -Kr - ZeE^{loc} \tag{2.18}$$

where m is mass of the electron shell, K is the spring constant, and E^{loc} is the external electric field acting locally at the atom position. Expressing Eq. (2.18) in frequency domain, one finds that the induced dipole moment can be written as

$$\vec{p} = \frac{Ze^2}{m(\omega_0^2 - \omega^2)}\vec{E}^{loc} \tag{2.19}$$

A simple model to describe displacement polarizability consists of two ions, one with a positive charge e, one with a negative charge –e and separated by distance d. Forces on the ionic pair includes both long-range electrostatic force E^{loc}, and short-range forces between the ions that are approximately proportional to the distance $\vec{d}$ between ions. One can then write the equation of motion for the two ions as:

$$m_p\frac{d^2\vec{u}_p}{dt^2} = -k(\vec{u}_p - \vec{u}_n) + e\vec{E}^{loc}$$
$$m_n\frac{d^2\vec{u}_n}{dt^2} = -k(\vec{u}_n - \vec{u}_p) - e\vec{E}^{loc} \tag{2.20a, b}$$

where u_n and u_p denotes displacement of negative and positive ions. The relative displacement between ions $\vec{d}$ can be described by

$$\frac{d^2\vec{d}}{dt^2} = \frac{e}{M}\vec{E}^{loc} - \frac{k}{M}\vec{d} \tag{2.21}$$

where M is the effective mass of the ion pair and given by $M^{-1} = m_p^{-1} + m_n^{-1}$. Writing in frequency domain, the ionic displacement is given by $d = \frac{e\vec{E}^{loc}}{M(\omega_0^2-\omega^2)}$. The total polarizability is the sum of the above two polarizabilities.

Polarizability of the material can in turn relate to macroscopic dielectric constant. One should note that the above polarizabilities described are "local" within the material, and respond to local electric field E^{loc}. The local electric field at position r can relate to the macroscopic electric field via relation [40] $\vec{E}^{loc}(\vec{r}) = \frac{\epsilon+2}{3}\vec{E}(\vec{r})$. From constitutive relations $\vec{D} = \vec{E} + 4\pi\vec{P}$ and $\vec{D} = \epsilon\vec{E}$, one can write macroscopic polarization as $\vec{P}(\vec{r}) = \frac{\epsilon-1}{4\pi}\vec{E}(\vec{r})$, which can in turn be expressed in terms of polarizabilities inside a primitive cell as $\vec{P}(\vec{r}) = \frac{\alpha}{v}\vec{E}^{loc}$, where v is the volume of a primitive cell. After rearranging above equations, one finds that dielectric constant of a material relates to the sum of microscopic polarizabilities of ionic pairs and atoms by

$$\frac{\epsilon - 1}{\epsilon + 2} = \frac{4\pi\alpha}{3v} \tag{2.22}$$

Equation (2.22) is the famous Clausius-Mossoti relation, which accounts for contributions to dielectric constant from microscopic atomic polarizabilities and ion displacement. This is saying

that macroscopic dielectric properties can be described from microscopic behaviors within a unit cell; this is generally true for dielectrics, but does not usually hold for metals. Clausius-Mossoti relation is evident in a number of fields. For example, when describing localized surface plasmons near a particle vs. a plane surface or when describing dielectrophoretic force.

In order to derive the Lorentz model fully, one substitutes polarizaiblity in Eq. (2.22) with the sum of atomic polarizability and polarizability from ionic displacements. Writing out the equation, one gets

$$\frac{\epsilon(\omega)-1}{\epsilon(\omega)+2}=\frac{4\pi}{3v}(\alpha_p+\alpha_n+\frac{e^2}{M(\omega_0^2-\omega^2)}) \tag{2.23}$$

which can be simplified using ϵ_∞ and ϵ_0, which are dielectric constant at infinite frequency and static electric field. Eq. (2.23) can be simplified to a Lorentz model without damping, where ω_T turns out to be the transverse optical phonon frequency:

$$\epsilon(\omega)=\epsilon_\infty+\frac{\epsilon_\infty-\epsilon_0}{(\omega^2/\omega_T^2)-1}$$
$$\omega_T^2=\omega_0^2\frac{\epsilon_\infty+2}{\epsilon_0+2} \tag{2.24}$$

One can relate the physical picture of atomic vibrations (phonons) to dielectric constant of a Lorentz model. For longitudinal optical phonons, wavevector k of lattice waves is parallel to polarization P, because it is atom displacements that generate polarizations P within the material. For transverse optical phonons, however, wavevector is perpendicular to polarization P.

Based on constitutive relations for electromagnetic response inside a material, two conditions also must satisfy:

- $\vec{k}\cdot\vec{P}=0$ or $\vec{D}=0$
- $\vec{k}\times\vec{P}=0$ or $\vec{E}=0$

In transverse modes, $\vec{k}$ is perpendicular to $\vec{P}$, satisfying the fist condition, therefore $\vec{E}$ must always vanish to satisfy the second condition, making dielectric constant go to infinity. Looking at Eq. (2.24), dielectric constant indeed goes to infinity at transverse phonon frequencies. Similarly, for longitudinal optical phonons, the dielectric constant is zero, because k is transverse to P, and for condition (1) to satisfy, it must be that $\vec{D}=0$ [40] . Since the longitudinal optical phonon frequency is when dielectric constant is zero, one can use Eq. (2.24) to relate transverse phonon frequencies and longitudinal phonon frequencies by the Lyddane-Sachs-Teller relation

$$\frac{\omega_L^2}{\omega_T^2}=\frac{\varepsilon_0}{\varepsilon_\infty} \tag{2.25}$$

Lyddane-Sachs-Teller relation describes the ratio of dielectric constant in short and long wavelength, as proportional to the ratio between longitudinal optical phonon frequency and transverse optical phonon frequency. Following the above derivation, this relation holds true for diatomic ionic crystals, but it is also generally true for many crystals. Using Lyddane-Sachs-Teller relation and Eq. (2.24), a simple Lorentz dielectric model is defined and shown in Fig. 2.2.

$$\varepsilon(\omega)=\varepsilon_{\infty}\left(1+\frac{\omega_T^2-\omega_L^2}{\omega^2-\omega_T^2}\right) \tag{2.26}$$

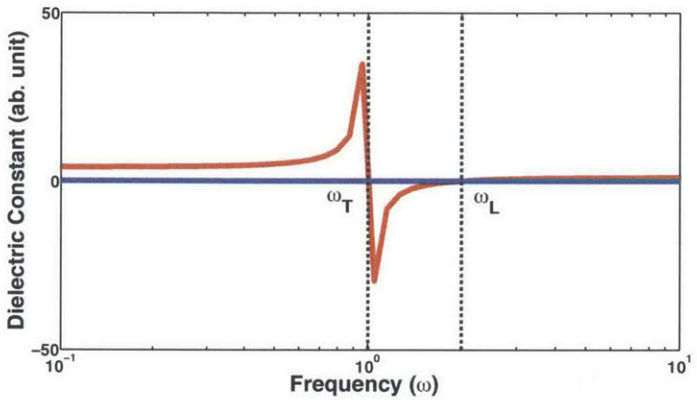

Figure 2.2: Lorentzian Dielectric model without damping

The dielectric constant is plotted with damping in Figure 2.3 below to illustrate its physical picture. If there is no damping with $\gamma=0$, the dielectric constant looks as in Figure **2.2**. At resonance frequency $\omega_0=\omega_T$, the dielectric constant goes to ∞. At longtidunal phonon frequency frequency, the dielectric constant goes to 0. The dielectric constant is purely real, and no absorption/loss is accounted for. Adding in damping makes imaginary part of the dielectric constant non-zero, and thus absorbing. Writing it in terms of ω_L and ω_T, the damped Lorentz response is typically

$$\varepsilon(\omega)=\varepsilon_{\infty}\frac{\omega^2-\omega_{LO}^2+i\gamma\omega}{\omega^2-\omega_{TO}^2+i\gamma\omega} \tag{2.27}$$

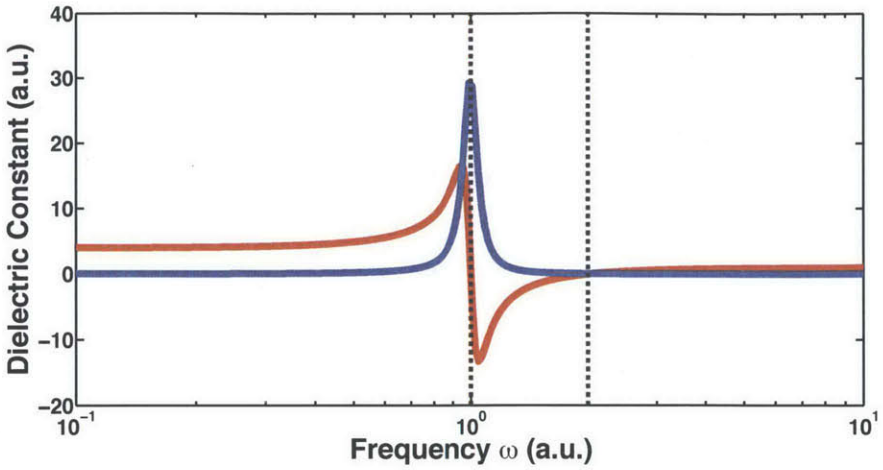

Figure 2.3: Lorentz Model with Damping

Another useful relationship for describing dielectric dispersion of a material is the Kramer-Kronig relation. Kramer-Kronig relation describes causality of the material response to external electric field. Kramer-Kronig relation is a general mathematical relation that relates real and imaginary part of an analytic equation in the upper-half plane. In a physical system, imaginary part of the response function to a small perturbation describes dissipation, since the system is out of phase with the driving force. Real part of the response function describes the reactions to the driving force. Kramer-Kronig relation simply means given dissipation or reaction of the system, we can deduce on or the other. Real physical systems are causal and thus analytical.

$$
\begin{aligned}
n(\omega) &= 1 + P\int_{-\infty}^{\infty} \frac{d\omega'}{\pi}\frac{k(\omega')}{\omega' - \omega} \\
k(\omega) &= -P\int_{-\infty}^{\infty} \frac{d\omega'}{\pi}\frac{n(\omega') - 1}{\omega' - \omega}
\end{aligned}
\tag{2.28}
$$

where P is a constant which makes sure of normalization. Usually given reflection data in enough frequency ranges, one can interpolate to find the refractive indices.

In mathematics, Titchmarsh theorem is the same as Kramer-Kronig relation which says that the real and imaginary part of the causal system's frequency response function are Hilbert transforms of one another[50].

4 Surface Waves at the Interface: Surface Phonon Polaritons and Total Internal Reflection

As mentioned in Chapter 1, surface wave is the major source of enhanced heat transfer at separation distances d smaller than the characteristic emission wavelength. As described in Section 1.2, two types of surface waves exist at the interface of the material and its surrounding medium: surface polaritons and total internally reflected waves. Surface polaritons consist of both surface plasmons typically in visible range and surface phonon polaritons typically in IR range. The author also notes that total internal reflected waves only exist on the low refractive-index side of an interface, while surface polaritons exist on both sides of the interface.

The following paragraphs will describe origins of surface phonon polaritons, but do not go into details for surface plasmons. This is because in surface plasmons, electrons interact resonantly with photons, whereas in surface phonon polaritons, phonons interact resonantely with photons. One cannot use the same physical picture to describe surface plasmon and surface phonon polariton. Before looking at surface phonon polaritons, the author first starts with a closer look at bulk phonon polaritons.

Phonon polaritons were first considered theoretically in 1950 by Ukranian physicist Kirill Tolpygo [39] when he derived relation between lattice vibrations and the dielectric constant. Before Tolpygo, Born theory was widely used to describe interaction of photons with lattice vibrations, which assumes that only nuclei positions of ionic pairs inside the crystal affect the dielectric dispersion. Tolpygo pointed out that deformation of electron clouds due to lattice vibrations is not negligible and demonstrated that in the long-wavelength limit, when lattice vibrations reach lots of neighbors, the dielectric dispersion is significantly different from predictions by Born theory. Tolpygo first termed these mixed modes between light and ionic vibrations as "light excitons", which are termed "polaritons" today[39].

Phonon polaritons received renewed interest after 1990s, due to an increasing interest in terahertz range applications for signal processing and communication systems. Polaritons here are proposed as signal carriers and the Nelson group at MIT showed that polaritons can be imaged, reflected, transmitted and controlled [42] using a pump-probe system. The primary medium for exciting phonon polaritons is ferroelectric materials, since they have large electro-optic coefficients. Energy inside the pump laser can be transferred to electronic or ionic vibrations inside the crystal [41]. Feurer et al. uses the large electro-optic coefficient of ferroelectrics to image the polaritons inside the crystal. The authors look at how atomic vibrations change optical constants of the material, which in turn is captured by the probe laser measurements.

In essence, phonon polariton is a form of excitation that couples phonons and photons. The coupling occurs because the zone-center optical phonons are at the same frequency and wavevector of photons. Therefore, a strong coupling between two modes exist; avoided crossing occurs and results in a peculiar dispersion relation in ω–k space. In a particular frequency range,

phonon polaritons behave similar to phonons and have a flat $\omega-k$ relation ($\omega=\omega_{phonon}$ for all k values). The phonon dispersion relation is flat because phonons have much larger wavevectors than photons, and therefore the dispersion looks flat compared with photon dispersion relation $\omega=ck$. At other frequencies, phonon polaritons behave like photons and is asymptotic to the light line.

In calculating the propagation of transverse electromagnetic waves inside the crystal, the simple equation $\varepsilon(\omega)=k^2c^2/\omega^2$ is used. The dispersion relation of bulk phonon polaritons can be derived by plugging in Lorentz model $\varepsilon(\omega)$, and is shown in Fig. 2.4.

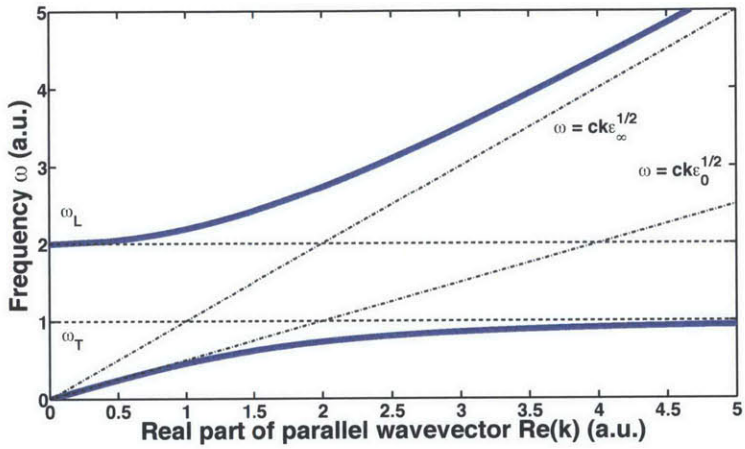

Figure 2.4: Dispersion Relation for Bulk Phonon Polaritons of a Lorentz Dielectric Material without Losses

As shown in Figure 2.4, the upper branch is asymptotic to $\omega=kc/\sqrt{\varepsilon_\infty}$ at higher frequencies, and behave like photons. When the wave vector becomes 0, the frequency goes to ω_L and behave like phonons. For lower branch, it is asymptotic to $\omega=kc/\sqrt{\varepsilon_0}$ at low frequencies but level off to ω_T as wave vector k is large.

As evident from Figure 2.4, electromagnetic waves with frequencies between longitudinal phonon and transverse phonon frequencies cannot propagate inside the material, since the dielectric constant of the crystal is negative. In this region, the wave vector k is purely imaginary, and the waves are diffusive and decaying. This frequency gap between longitudinal phonon and transverse phonon exists because optical phonon frequencies of ionic crystals split at zone-center. Splitting of optical phonon frequencies is a general property of polar materials, in which positive and negative charges naturally separate. The splitting occurs because long-range electrostatic forces act in different ways when the material experiences a transverse or a longitudinal lattice wave in long-wavelength limit. The longitudinal local fields act to reduce polarization and adds to the restoring forces locally, thus the frequency of vibrations is pushed up. The transverse local fields act to increase polarization and reduces the restoring forces locally, thus frequency of vibrations is pushed down [40].

Similarly, one can plug in the Lorentz model with damping and plot the dispersion relation of bulk phonon polaritons inside a lossy dielectric.

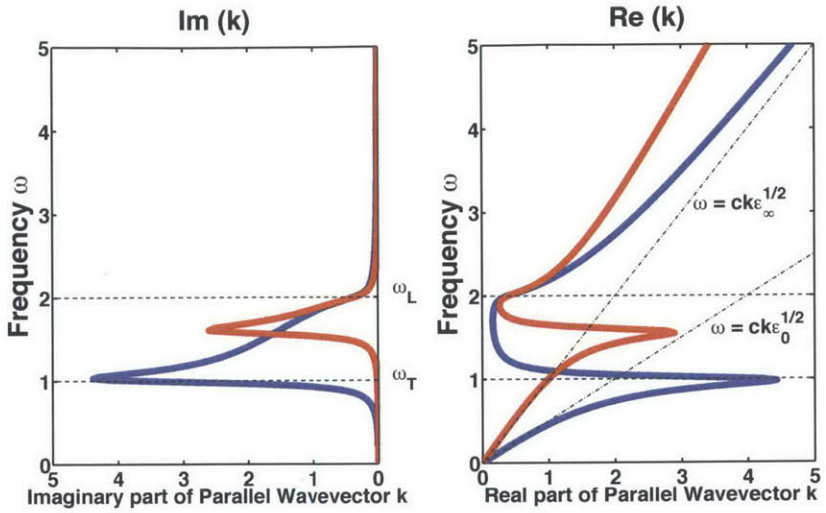

Figure 2.5: Dispersion Relation for Lorentz Model with Damping

One can also estimate the frequency range of phonon polaritons by looking at vibrational modes within the crystal. Vibrational modes are typically excited at energies $3/2k_BT$. At room temperatures, this frequency corresponds $3/2\times(8.62*10^{-5}eVK^{-1})*300K\approx0.03eV$, which indeed falls in the terahertz range.

Phonon polaritons can also exist at the surface of the material, in addition to inside the material. It can be viewed as a counterpart of surface plasmon polaritons in the IR range. The existence of such surface waves is only valid when real part of the dielectric constant becomes negative of that of its surrounding medium. Microscopically, local polarizability of the material defined from local fields inside the material, is inversely proportional to the sum of dielectric constants of material and its surrounding medium [40]. Thus when the sum of dielectric constants become zero in real-space, leaving only imaginary components, the material has an infinite local polarizability and strongly absorbs due to the purely imaginary polarizability.

The dispersion relation of surface phonon polaritons is derived by matching boundary conditions of Maxwell equations at the interface, assuming the existence of an evanescently decaying surface wave in the out-of-plane direction [42]. The dispersion relation for surface phonon polaritons is given as

$$k=\frac{\omega}{c}\sqrt{\frac{\varepsilon_1\varepsilon_2}{\varepsilon_1+\varepsilon_2}} \tag{2.29}$$

Fig. 2.6 plots surface phonon polaritons of a lorentz material with its bulk phonon polaritons. As observed from graph, horizontal part of surface phonon polariton dispersion exist at a

frequency between ω_T and ω_L. In contrast, horizontal and "phonon-like" part of bulk phonon polaritons exist at frequencies ω_T and ω_L.

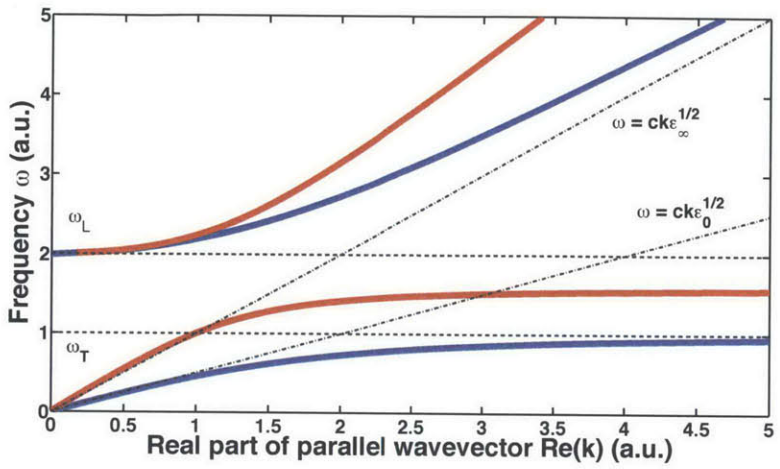

Figure 2.6: Dispersion Relation for Bulk Phonon Polariton and Surface Phonon Polaritons of a Lorentz Material Without Losses

The physical picture of the surface phonon polaritons and surface plasmons is still an active topic for current research. Researchers are using different analytical and numerical methods to study physics of these surface waves, such as quantum mechanics, finite difference time domain (FDTD) methods.

Total internal reflection also produces surface waves. It is most evident by matching electric field $\vec{E}$ and magnetic field $\vec{H}$ at the interface of two materials. Total internal reflection happens when light shines from high index material to low index material, and when high-index parallel wave vector exceeds maximum allowable wave vector in the low index media, specifically when $k_{|}^{high} > \frac{\omega}{c}\sqrt{\varepsilon_{low}}$. The dispersion relation for decaying evanescent fields is given by $k_{\perp} = \pm i\sqrt{k_{|,high}^2 - (\frac{\omega}{c})^2 \varepsilon_{low}}$ and the out-of-plane wavevector is always imaginary.

One major difference between surface phonon polariton (SPP) waves and total internal reflected (TIR) waves is that SPP waves extend on both sides of the interface, while TIR waves exist only on the side of low-index material. Other differences between the two are not related to topic of the thesis, and will not be detailed.

5 Dyadic Green's Function for Parallel Half-Spaces

In this section, Green's function is solved for parallel planar media. A special case is then parallel half spaces, which is of primary interest for us. The main reference is Professor Jin Au Kong's

notes [45] for his advanced electromagnetics class course 6.635 at MIT. The lecture note can be found online on MIT OpenCourseWare.

Wave solutions for parallel planar media is simply a superposition of plane waves that would normally exist in free space. How these plane waves are superimposed is determined by the boundary conditions. The first step is to expand Green's function in terms of plane waves in k-space. Note that in the end, only an implicit form for the Green's function is obtained as an integral of plane waves over k-space. Writing it in explicit form is very difficult and not worth trying for the purpose of calculating energy flow.

Step 0: Relating Dyadic form to Scalar form Dyadic form of Green's function can be related to its scalar form, since scalar forms are easier to solve. This dyadic form has dimension 3x3, and considers coupling of field and source in different directions. Scalar form is 1x1 and only deals with coupling of field and source in the same direction. We know that scalar Green's function satisfies equation

$$(\nabla^2 + k_0^2)g(\vec{r}, \vec{r'}) = -\delta(\vec{r} - \vec{r'}) \tag{2.30}$$

where $\vec{r}$ and $\vec{r}$' are positions of field and source respectively. The dyadic Green's function satisfies this dyadic Maxwell equation

$$\nabla \times \nabla \times \bar{\bar{G}}(\vec{r}, \vec{r'}) - k_0^2 \bar{\bar{G}}(\vec{r}, \vec{r'}) = \bar{\bar{I}}\delta(\vec{r} - \vec{r'}) \tag{2.31}$$

Therefore the Dyadic Green's function can relate to the scalar form as

$$\bar{\bar{G}}(\vec{r}, \vec{r'}) = (\bar{\bar{I}} + \tfrac{1}{k_0^2}\nabla\nabla)g(\vec{r}, \vec{r'}) \tag{2.32}$$

Its correctness can be verified by plugging the dyadic Green's function into the dyadic Maxwell equations

$$\begin{aligned}
&\nabla \times \nabla \times \bar{\bar{I}}g(\vec{r}, \vec{r'}) + \nabla \times \nabla \times (\frac{1}{k_0^2}\nabla\nabla g) - k_0^2(\bar{\bar{I}}g + \frac{1}{k_0^2}\nabla\nabla g) \\
&= \nabla\nabla g - \nabla \cdot (\nabla g)\bar{\bar{I}} + \frac{1}{k_0^2}(\nabla \times \nabla \times \nabla\nabla g) - k_0^2\bar{\bar{I}}g - \nabla\nabla g \\
&= -(\nabla^2 g\bar{\bar{I}} + k_0^2\bar{\bar{I}}g) + 0 \\
&= \bar{\bar{I}}\delta(\vec{r} - \vec{r'})
\end{aligned}$$

where vector identities $\nabla\times\nabla\times(Ig)=\nabla\nabla g-\nabla\cdot(\nabla g)I$ are used and that taking curl of a gradient field is always 0.

Step 1: Expand Green's function in k-space The scalar Green's function can be expanded in k-space using Fourier expansion and obtain equations

$$g(\vec{r}, \vec{r'}) = \tfrac{1}{(2\pi)^3}\int\int\int_{-\infty}^{+\infty} d\vec{k}e^{i\vec{k}\cdot(\vec{r}-\vec{r'})}g(\vec{k}) \tag{2.33}$$

$$\delta(\vec{r}-\vec{r}') = \frac{1}{(2\pi)^3}\int\int\int_{-\infty}^{+\infty} d\vec{k}e^{i\vec{k}\cdot(\vec{r}-\vec{r}')} \tag{2.34}$$

Plugging into the Helmholtz equation, the equation becomes

$$\begin{aligned}(\nabla^2+k_0^2)\int\int\int_{-\infty}^{+\infty} d\vec{k}e^{i\vec{k}\cdot(\vec{r}-\vec{r}')}g(\vec{k}) &= -\int\int\int_{-\infty}^{+\infty} d\vec{k}e^{i\vec{k}\cdot(\vec{r}-\vec{r}')} \\ &= \int\int\int_{-\infty}^{+\infty} d\vec{k}((i\vec{k})^2+k_0^2)e^{i\vec{k}\cdot(\vec{r}-\vec{r}')}g(\vec{k}) \\ &= \int\int\int_{-\infty}^{+\infty} d\vec{k}(-k_x^2-k_y^2-k_z^2+k_0^2)e^{i\vec{k}\cdot(\vec{r}-\vec{r}')}g(\vec{k})\end{aligned}$$

which just gives a general expression for $g(\vec{k})$

$$g(\vec{k}) = \frac{1}{k_x^2+k_y^2+k_z^2-k_0^2} \tag{2.35}$$

That is to say, the Green's function in real-space is an integral in the form $\int dkg(k)$. The Green's function can be further integrated over $d\vec{k}_{\|}$ or the parallel wave vector to the interface to get a simplified form . The integration over k_z involves the use of Cauchy theorem in complex analysis, which gives

$$\begin{aligned}\int_{-\infty}^{+\infty} dk_z \frac{1}{k_z^2-k_{z0}^2}e^{i\vec{k}\cdot(\vec{r}-\vec{r}')} &= 2i\pi Res\left[\frac{1}{k_z^2-k_{z0}^2}e^{i\vec{k}\cdot(\vec{r}-\vec{r}')}\right] \\ &= 2i\pi\frac{1}{2k_{z0}}e^{i\vec{k}\cdot(\vec{r}-\vec{r}')}\end{aligned} \tag{2.36}$$

There are two main theorems used at this step, the Cauchy integral theorem and the Residue theorem. No matter the k_{z0} is purely real or purely complex, depending on this is propagating or evanescent wave respectively, the integration is always from $-\infty$ to $+\infty$ by taking a half-circle contour going from $x = -\infty$ to $x = +\infty$ on the real axis, then completing an infinitely large half circle on the upper half complex plane or lower half complex plane. There are either two poles on the real axis, or two poles on the imaginary axis. If pole is on the imaginary axis, this contour integral yields $2i\pi Res(f(z))$ as z approaches the imaginary pole; or the contour integral yields $i\pi Res(f(z=k_{z0}))+(-i\pi Res(f(z=-k_{z0})))$ for $k_{z0}>0$. The integrals are equal no matter which integration path is taken.

The integral over the infinitely large half circle not including the real axis, is always zero. That is to say, the integral we are interested in is equal to $2i\pi Res(f(z))$, that is $2\pi i$ times residue of the function.

The residue of the function can be calculated using L'opital's rule as below

$$Res(f(z=z_0)) = \lim_{z\to z_0} f(z)(z-z_0) \tag{2.37}$$

So the final scalar Green's function is

$$g(\vec{r},\vec{r}') = \frac{i}{(2\pi)^2}\int\int_{-\infty}^{\infty} d\vec{k}_{\parallel}\frac{1}{2k_{z0}}e^{ik_{\parallel}\cdot(\vec{r}_{\parallel}-\vec{r}'_{\parallel})}e^{ik_{z0}(z-z')} \tag{2.38}$$

for $z-z'>0$, where $k_{\parallel}$ corresponds to $k_x\hat{i}_x + k_y\hat{i}_y$ and $k_{z0}^2 = k_0^2 - k_x^2 - k_y^2$.

We should also note that Cauchy integration cannot work if the function is divergent, which means that $\lim_{k_z\to\infty} e^{ik_z z} < +\infty$. That is to say for $z>0$, the imaginary part of k_z needs to be positive; vice versa for $z<0$.

For $z<0$, we follow the same process and get

$$g(\vec{r},\vec{r}') = \frac{i}{(2\pi)^2}\int\int_{-\infty}^{\infty} d\vec{k}_{\parallel}\frac{1}{2k_{z0}}e^{ik_{\parallel}\cdot(\vec{r}_{\parallel}-\vec{r}'_{\parallel})}e^{ik_{z0}|z-z'|} \tag{2.39}$$

for any $z-z'$ on the real line.

Step 2: Transform scalar Green's function to Dyadic form

The next step is to transform the scalar Green's function to its Dyadic form using the equations derived in Step 1 above. This step is straightforward with the use of tensor operations. However, when taking gradient of the scalar field, special attention needs to be paid to the z = 0 case, since the function is discontinuous at z = 0 due the absolute value $|z-z'|$.

For $z>0$, Eq. 2.21 is used to calculate the Dyadic Green's function. Here $e^{ik_{z0}|z|} = e^{ik_{z0}z}$, thus

$$\frac{\partial}{\partial x}\frac{\partial}{\partial x}e^{i(k_x x+k_y y)}e^{ik_{z0}z}\hat{x}\hat{x} = -k_x^2 e^{i(k_x x+k_y y+k_{z0}z)}\hat{x}\hat{x} \tag{2.40}$$

$$\frac{\partial}{\partial x}\frac{\partial}{\partial y}e^{i(k_x x+ik_y y)}e^{ik_{z0}z}\hat{x}\hat{y} = -k_x k_y e^{i(k_x x+k_y y+k_{z0}z)}\hat{x}\hat{y} \tag{2.41}$$

$$\frac{1}{k_{z0}^2}\nabla\nabla g = (-1)\frac{i}{8\pi^2}\int\int_{-\infty}^{\infty} d\vec{k}_{\parallel}\frac{1}{k_{z0}}\times \frac{(k_x^2\hat{x}\hat{x} + k_x k_y\hat{x}\hat{y} + k_x k_{z0}\hat{x}\hat{z}_0 + k_y k_x\hat{y}\hat{x} + k_y^2\hat{y}\hat{y} + k_y k_{z0}\hat{y}\hat{z}_0 + k_{z0}k_x\hat{z}_0\hat{x} + k_{z0}k_y\hat{z}_0\hat{y} + k_{z0}^2\hat{z}_0 hat_{z_0})}{k_0^2}e^{i\vec{k}\cdot\vec{r}} \tag{2.42}$$

For $z>0$ it yields

$$\frac{1}{k_{z0}^2}\nabla\nabla g = \frac{i}{8\pi^2}\int\int_{-\infty}^{\infty} d\vec{k}_{\parallel}\frac{1}{k_{z0}}\frac{-\vec{k}\vec{k}}{k_0^2}e^{i\vec{k}\cdot\vec{r}} \tag{2.43}$$

where $\vec{k} = k_x\hat{x} + k_y\hat{y} + k_z\hat{z}$.

For z = 0 case, however,

$$\frac{\partial^2}{\partial z^2}e^{ik_{z0}|z|} = \frac{\partial}{\partial z}\left\{ik_{z0}e^{ik_{z0}|z|}\frac{\partial}{\partial z}|z|\right\}$$

$$=ik_{z0}\left\{ik_{z0}e^{ik_{z0}|z|}\left(\frac{\partial}{\partial z}|z|\right)^2+ik_{z0}e^{ik_{z0}|z|}\frac{\partial^2}{\partial z^2}|z|\right\}$$

$$=2ik_{z0}\delta(z)-k_{z0}^2e^{ik_{z0}|z|}$$

The second derivative of g over z is given as

$$\begin{aligned}\frac{\partial^2}{\partial z^2}g(\vec{r}) &= \frac{i}{(2\pi)^2}\int\int_{-\infty}^{\infty}d\vec{k}_{\|}\frac{1}{2k_{z0}}e^{i\vec{k}_{\|}\cdot\vec{r}_{\|}}\left[2ik_{z0}\delta(z)-k_{z0}^2]e^{ik_{z0}|z|}\right] \\ &= -\frac{\delta(z)}{(2\pi)^2}\int\int_{-\infty}^{\infty}d\vec{k}_{\|}e^{i\vec{k}_{\|}\cdot\vec{r}_{\|}}-\frac{i}{8\pi^2}\int\int_{-\infty}^{\infty}d\vec{k}_{\|}k_{z0}e^{i\vec{k}_{\|}\cdot\vec{r}_{\|}}e^{ik_{z0}|z|} \\ &= -\delta(\vec{r})-\frac{i}{8\pi^2}\int\int_{-\infty}^{\infty}d\vec{k}_{\|}k_{z0}e^{i\vec{k}_{\|}\cdot\vec{r}_{\|}}e^{ik_{z0}|z|}\end{aligned}$$

The Dyadic Green's function thus can be written as, for z > 0

$$\bar{\bar{G}}(\vec{r},\vec{r}') = -\hat{z}\hat{z}\frac{\delta(\vec{r})}{k_0^2}+\frac{i}{8\pi^2}\int\int_{-\infty}^{\infty}d\vec{k}_{\|}\frac{1}{k_{z0}}\left[\bar{\bar{I}}-\frac{\vec{k}\vec{k}}{k_0^2}\right]e^{i\vec{k}\cdot\vec{r}} \tag{2.44}$$

$$\bar{\bar{G}}(\vec{r},\vec{r}') = -\hat{z}\hat{z}\frac{\delta(\vec{r})}{k_0^2}+\frac{i}{8\pi^2}\int\int_{-\infty}^{\infty}d\vec{k}_{\|}\frac{1}{k_{z0}}\left[\bar{\bar{I}}-\frac{\vec{K}\vec{K}}{k_0^2}\right]e^{i\vec{K}\cdot\vec{r}} \tag{2.45}$$

where the second equation is for waves traveling in –z direction and

$$\begin{aligned}\vec{k} &= k_x\hat{x}+k_y\hat{y}+k_{z0}\hat{z} \\ \vec{K} &= k_x\hat{x}+k_y\hat{y}-k_{z0}\hat{z}\end{aligned} \tag{2.46}$$

Step 3: Relating to TE and TM modes

The above equation decomposes the fields into x, y and z directions. In principal, the fields can be decomposed into any orthonormal set of vectors as long as the set is self-consistent. Based on TE and TM polarization, a new orthonormal system can be defined:

$$TE:\hat{e}(k_{z0}) = \frac{\vec{k}\times\hat{z}}{\left[\vec{k}\times\hat{z}\right]} = \frac{1}{\sqrt{k_x^2+k_y^2}}\left[\hat{x}k_y-\hat{y}k_x\right] = \frac{1}{k_\rho}(\hat{x}k_y-\hat{y}k_x)$$

$$TM:\hat{h}(k_{z0}) = \frac{1}{k_0}\hat{e}(k_{z0})\times\vec{k} = -\frac{k_{z0}}{k_0k_\rho}(\hat{x}k_y+\hat{y}k_x)+\frac{k_\rho}{k_0}\hat{z}$$

(2.47)

The unit vectors $\hat{k}$, $\hat{h}$ and $\hat{e}$ does form an orthonormal set, such that the Green's function can be expressed in terms of this new orthonormal set:

$$\bar{\bar{G}}(\vec{r},\vec{r}') = -\hat{z}\hat{z}\frac{\delta(\vec{r})}{k_0^2} + \frac{i}{8\pi^2}\int\int_{-\infty}^{\infty} d\vec{k}_{\parallel}\frac{1}{k_{z0}}\left[\hat{e}(k_{z0})\hat{e}(k_{z0}) + \hat{h}(k_{z0})\hat{h}(k_{z0})\right]e^{i\vec{k}\cdot(\vec{r}-\vec{r}')} \tag{2.48}$$

$$\bar{\bar{G}}(\vec{r},\vec{r}') = -\hat{z}\hat{z}\frac{\delta(\vec{r})}{k_0^2} + \frac{i}{8\pi^2}\int\int_{-\infty}^{\infty} d\vec{k}_{\parallel}\frac{1}{k_{z0}}\left[\hat{e}(-k_{z0})\hat{e}(-k_{z0}) + \hat{h}(-k_{z0})\hat{h}(-k_{z0})\right]e^{i\vec{K}\cdot(\vec{r}-\vec{r}')} \tag{2.49}$$

where

$$\hat{e}(-k_{z0}) = \hat{e}(k_{z0})$$
$$\hat{h}(-k_{z0}) = \frac{\hat{e}(-k_{z0})\times\vec{K}}{k_0} \tag{2.50}$$

Step 4: Boundary conditions and Coefficients

The final expression for dyadic Green's function above relates clearly to the physical picture. There are two waves propagating, one at +z and one at -z direction. Depending on the direction at which the source is radiating, additional coefficients can be specified based on boundary conditions.

From Step 3, $\hat{e}(k_{z0})$ denotes TE waves traveling in the positive z direction, and $\hat{h}(k_{z0})$ denotes TM waves traveling in positive z direction. While $\hat{e}(-k_{z0})$ denotes TE waves traveling in the negative z direction, and similarly for $\hat{h}(-k_{z0})$.

The terms in Green's function can be re-arranged to make sense of its physical meaning.

$$\bar{\bar{G}}(\vec{r},\vec{r}') = -\hat{z}\hat{z}\frac{\delta(\vec{r})}{k_0^2} + \frac{i}{8\pi^2}\int\int_{-\infty}^{\infty} d\vec{k}_{\parallel}\frac{1}{k_{z0}}\left\{\left[\hat{e}(k_{z0})e^{i\vec{k}\cdot\vec{r}}\right]\hat{e}(k_{z0})e^{-i\vec{k}\cdot\vec{r}'} + \left[\hat{h}(k_{z0})e^{i\vec{k}\cdot\vec{r}}\right]\hat{h}(k_{z0})e^{-i\vec{k}\cdot\vec{r}'}\right\}$$

(2.51)

for $z>z'$, or traveling in positive z direction for a source that emits in +z direction.

$$\bar{\bar{G}}(\vec{r},\vec{r}') = -\hat{z}\hat{z}\frac{\delta(\vec{r})}{k_0^2} + \frac{i}{8\pi^2}\int\int_{-\infty}^{\infty} d\vec{k}_{\parallel}\frac{1}{k_{z0}}\left\{\left[\hat{e}(-k_{z0})e^{i\vec{K}\cdot\vec{r}}\right]\hat{e}(-k_{z0})e^{-i\vec{K}\cdot\vec{r}'} + \left[\hat{h}(-k_{z0})e^{i\vec{K}\cdot\vec{r}}\right]\hat{h}(-k_{z0})e^{-i\vec{K}\cdot\vec{r}'}\right\}$$

(2.52)

for $z<z'$, or traveling in negative z direction for a source that emits in -z direction. Note that terms with $e^{i\vec{k}\cdot\vec{r}}$ in brackets describes the field, whereas the terms with $e^{i\vec{k}\cdot\vec{r}'}$ describes the source. But in a multi-layer system (in this case, 3 layers), there are multiple reflections and transmissions that will allow sources that emit in +z direction to generate waves traveling in -z direction. To capture reflections, Transfer-Matrix Method (TMM) is used to rewrite the equation for the case when the source and field are not in the same layer:

$$\bar{\bar{G}}(\vec{r},\vec{r}') = \frac{i}{8\pi^2}\int\int_{-\infty}^{\infty} d\vec{k}_{\parallel}\frac{1}{k_{z0}}\left\{\vec{K}_e^-\hat{e}(-k_{z0})e^{-i\vec{K}\cdot\vec{r}'} + \vec{K}_h^-\hat{h}(-k_{z0})e^{-i\vec{K}\cdot\vec{r}'} + \vec{K}_e^+\hat{e}(k_{z0})e^{-i\vec{k}\cdot\vec{r}'} + \vec{K}_h^+\hat{h}(k_{z0})e^{-i\vec{k}\cdot\vec{r}'}\right. \tag{2.53}$$

where the fields are divided into two types, fields originated from +z directed sources and -z directed sources. Coefficients can be added for these fields.

$$\begin{aligned}
\vec{K}_e^- &= A_l^{TE}\hat{e}(-k_{z0})e^{i\vec{K}\cdot\vec{r}} + B_l^{TE}\hat{e}(k_{z0})e^{i\vec{k}\cdot\vec{r}} \\
\vec{K}_h^- &= A_l^{TM}\hat{h}(-k_{z0})e^{i\vec{K}\cdot\vec{r}} + B_l^{TM}\hat{h}(k_{z0})e^{i\vec{k}\cdot\vec{r}} \\
\vec{K}_e^+ &= C_l^{TE}\hat{e}(-k_{z0})e^{i\vec{K}\cdot\vec{r}} + D_l^{TE}\hat{e}(k_{z0})e^{i\vec{k}\cdot\vec{r}} \\
\vec{K}_h^- &= C_l^{TM}\hat{e}(-k_{z0})e^{i\vec{K}\cdot\vec{r}} + D_l^{TM}\hat{e}(k_{z0})e^{i\vec{k}\cdot\vec{r}}
\end{aligned}$$

(2.54)

where A_l^{TE} describes amplitude of TE polarized field traveling in -z direction originated from -z directed source without reflections. Similarly, B_l^{TE} describes amplitude of TE polarized field traveling in +z direction originated from -z directed source with reflections.

6 Fluctuation-Dissipation Theorem

Fluctuation of electromagnetic fields is derived under the big umbrella of linear response theory. Linear response theory describes non-equilibrium systems and its behavior. Fluctuation-dissipation theorem in general relates dissipation in a non-equilibrium system to the fluctuations occurring at different times in equilibrium systems. It is important for understanding fluctuating fields, especially at nanoscale near very small objects.

To derive it fully Fermi's golden rule needs to be used and quantum correlation functions need to be evaluated. However, to see its physical meaning, a more classical approach outlined in book [46] can be used.

Assume a reservoir of N charged particles, for state s of the system, its dipole moment μ(s) has probability distribution function

$$f_{eq}(s)=f_0 e^{-H_0(s)/kT} \tag{2.55}$$

where H_0 is the equilibrium Hamiltonian of the system. The ensemble average of dipole moment at time t is:

$$\langle\vec{\mu}(s,t)\rangle = \frac{\int f_{eq}(s)\vec{\mu}(s,t)ds}{\int f_{eq}(s)ds} \tag{2.56}$$

Consider an external electric field $\vec{E}(\vec{r},t)$ which acts as a perturbation. A few assumptions before the derivations include:

- The external electric field acts on the dipole at time *t* is $\vec{\mu}(s,t)$ and adds in additional energy.

- The system perturbation is so small that we can assume a linear response to the external field.
- The average change in the Hamiltonian $<\delta H(s)>$ is 0.
- The system is stationary, i.e. the response function only depends on the difference between times $(t-t')$.
- The system is causal.

The perturbed Hamiltonian is

$$H = H_0 + \delta H = H_0 - \vec{\mu}(s,t) \cdot \vec{E}(t) = H_0 - \sum_k \mu_{k=x,y,z}(s,t) E_k(t) \tag{2.57}$$

Assume a linear response α to perturbation $\vec{E}$ that is

$$\delta\mu_j(t) = \frac{1}{2\pi} \sum_k \int_{-\infty}^{t} \alpha_{jk}(t-t') E_k(t') dt' \tag{2.58}$$

The response function is found to be

$$\alpha_{jk}(t) = -\frac{2\pi}{E_k^0} \Theta(t) \frac{d}{dt} \delta\mu_j(t) \tag{2.59}$$

where $\Theta(t)$ is step function of time t.

The perturbed Hamiltonian can be plugged in to find δμ first, then use the above relation to find the linear response function α. Change in dipole moment δμ can be found as follows

$$f(s)=f_{eq}(s) \left[1-\frac{1}{kT}\delta H(s)+...\right] \tag{2.60}$$

where $\delta H(s)$ is the perturbation at time t = 0, for the system at thermal equilibrium at t = 0.

One can rewrite the dipole moment in terms of its ensemble average $\langle\vec{\mu}\rangle$ and other terms as,

$$\begin{aligned}
\vec{\mu}(t) &= \frac{\int f_{eq}(s)\vec{\mu}(s,t)ds - \int f_{eq}(s)\frac{1}{kT}\delta H(s)\vec{\mu}(s,t)ds}{\int f_{eq}(s)ds - \int f_{eq}(s)\frac{1}{kT}\delta H(s)ds} \\
&= \frac{<\vec{\mu}> - \frac{1}{kT}\langle\delta H(s)\vec{\mu}(s,t)\rangle}{1-\frac{<\delta H(s)>}{kT}} \\
&=<\vec{\mu}> + \frac{<\vec{\mu}><\delta H(s)> - <\delta H(s)\vec{\mu}(s,t)>}{kT - <\delta H(s)>} \\
&=<\vec{\mu}> + \frac{<\vec{\mu}><\delta H(s)> - <\delta H(s)\vec{\mu}(s,t)>}{kT}
\end{aligned}$$

Since $\delta H(s)$ is the perturbation at time t = 0, can be expanded and written as $-\sum_k \mu_k(s,0)E_k^0$.

The dipole moment at time t can be described in terms of the initial distribution function $f(s,t=0)$ because it is assumed that there is no states crossing in the time space, and that the states at time t can be described only from initial distribution at time zero.

Therefore,

$$\begin{aligned}\delta\vec{\mu}(t) &= \vec{\mu}(t) - <\vec{\mu}> \\ &= \frac{<\vec{\mu}><\delta H(s)> - <\delta H(s)\vec{\mu}(s,t)>}{kT} \\ &= -\frac{E_k^0}{kT}\left[<\mu_j(t)><\mu_k(0)> - <\mu_k(0)mu_j(t)>\right] \\ &= \frac{E_k^0}{kT}\langle[\mu_k(0) - <\mu_k>][\mu_j(t) - <\mu_j>]\rangle\end{aligned}$$

where the cross terms completely cancel out. This is to say the system response at time t can be described as a correlation between the system at t = 0 and the system at time t.

$$\alpha_{j,k}(t) = -\frac{2\pi}{kT}\Theta(t)\frac{d}{dt} < \delta\mu_k(0)\delta\mu_j(t) > \tag{2.61}$$

The equations can then be written in frequency domain.

$$\begin{aligned}\langle\delta\mu_j(\omega)\delta\mu_k*(\omega')\rangle &= \frac{1}{4\pi^2}\int\int_{-\infty}^{\infty}\langle\delta\mu_j(\tau')\delta\mu_k(\tau)\rangle\, e^{i[\omega\tau' - \omega'\tau]}d\tau' d\tau \\ &= \frac{1}{4\pi^2}\int\int_{-\infty}^{\infty}\langle\delta\mu_k(\tau)\delta\mu_j(t+\tau)\rangle\, e^{i[\omega-\omega']\tau}e^{i\omega t}d\tau dt \\ &= \delta(\omega-\omega')\frac{1}{2\pi}\int_{-\infty}^{\infty}\langle\delta\mu_k(\tau)\delta\mu_j(t+\tau)\rangle\, e^{i\omega t}dt\end{aligned}$$

$$\begin{aligned}\alpha_{jk}(\omega) &= -\frac{2\pi}{kT}\int\Theta(\omega-\omega')H(\omega')d\omega' \\ &= -\frac{2\pi}{kT}\int\frac{1}{2\pi}[\pi\delta(\omega-\omega') + \frac{i}{\omega-\omega'}]\times \\ &\left[\frac{2\pi i\omega}{\delta(\omega-\omega'')} < \delta\mu_j(\omega)\delta\mu_k^*(\omega'') >\right],\end{aligned}$$

$$\alpha_{jk}(\omega) - \alpha_{jk}(\omega)^* = -\frac{2\pi}{kT}2i\omega<\delta\mu_j(\omega)\delta\mu_k^*(\omega')>\frac{1}{\delta(\omega)-\delta(\omega')} \tag{2.62}$$

Taking the imaginary part of the response function α, the following sections deal with only real part of the Fourier transform of the step function τ(ω) because its imaginary part is undefined or divergent at ω=ω'. Note that there is a factor of 2 difference from the equation above to the equation in the reference.

To find the correlation function between currents denoted by j, this relation is used

$$\delta j = \frac{d}{dt}[\delta\mu]\delta(\vec{r}-\vec{r'}) \tag{2.63}$$

$$\delta j(\omega) = -i\omega\alpha(\omega)\delta(\vec{r}-\vec{r'})\delta E \tag{2.64}$$

where Eq. (2.63) relates the instantaneous velocity of electrons v and the time derivative of dipole moment μ. Eq. (2.64) is an extention from the definition of response function α.

The final expression for the fluctuation-dissipation theorem is in the form below

$$\langle \delta j_\alpha(\vec{r},\omega)\delta j_\beta(\vec{r'},\omega')\rangle = \frac{\omega\epsilon_0}{\pi}\epsilon''\Theta(\omega,T)\delta(\vec{r}-\vec{r'})\delta(\omega-\omega')\delta_{\alpha,\beta} \tag{2.65}$$

Here, j denotes the current fluctuations, where α,β denote directions x, y or z, ε_0 is the vacuum permittivity, ε'' is the imaginary part of the relative permittivity of the medium. The relative permittivity can be written as $\varepsilon=\varepsilon'+i\varepsilon''$. $\theta(\omega,T)$ is the average energy of a photon or Planck oscillator excited at temperature T at frequency ω, where $\Theta(\omega,T) = \frac{\hbar\omega}{e^{\frac{\hbar\omega}{kT}}-1}$.

Of course, the fluctuation dissipation is still an approximation, but a rather good one. Its physical meaning as well as limitations can be inferred.

First, the response is local due to $\delta(\vec{r}-\vec{r'})$term. Current fluctuations at different positions are uncorrelated. However, this breaks down in real life, because in essence there is always some correlation. When a charge is moved by external electric force at position r, it in turn moves the charges around it. This effect is usually small, but in highly non-local materials when the material's dielectric constant depends strongly on the wave vector k, the Fourier analog of space coordinate r, the fluctuation dissipation theory has to be modified.

Second, the response is linear due to term δ(ω−ω'). However, in some materials, if the electric field has frequency ω, it is also able to excite charge fluctuations at other frequencies. Meaning, if one charge oscillates at frequency ω, its surrounding charges will respond at frequencies other than ω.

Third, only the imaginary part of the dielectric constant comes in, because it's only the imaginary part that relates to dissipation within the material. This is similar to a damped oscillator. When there is no damping, the oscillator energy is conserved. Adding a damping and imaginary part of the response function leads to dissipation.

7 Reaching Final Expression

To find the total energy flow from one half-space to another parallel half-space, a few important points have to be outlined first. The figure shows again the configuration calculated for: parallel half spaces. The volumes of emitter and receiver both extend to infinity in x and y direction.

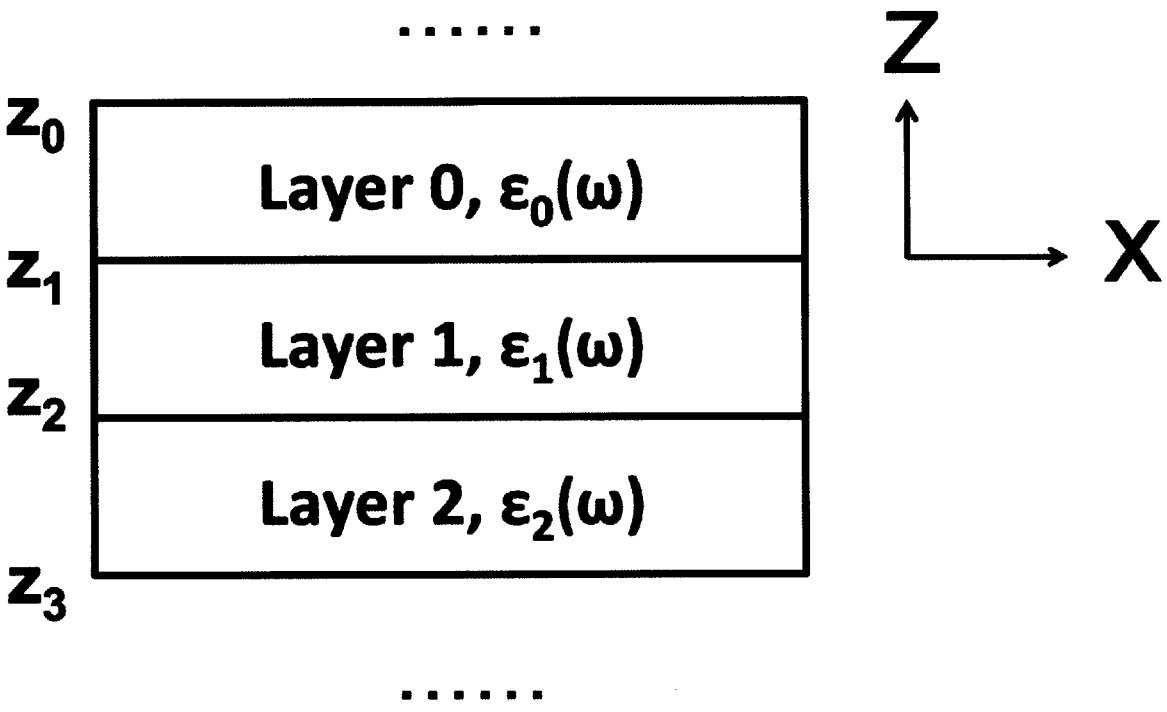

Figure 2.7: Parallel Half Spaces Configuration and Related Paramaeters

- Only energy flow in the direction perpendicular to the interfaces is interesting for the purpose of this thesis. So in considering Poynting vectors, only the cross-plane direction, not the parallel-plane direction, is considered. In considering the parallel plane direction, we can refer to paper [47].
- The source terms inside the Green's function should be entire volumes of both half spaces.
- The net energy flow can be described as the difference in energy flow between that at z = 0 and z = d.

Step 1: Writing in terms of Green's functions

The electric and magnetic fields can be written in terms of Green's function. As mentioned before, the average Poynting vector is equal to $\vec{S}(\vec{r},\omega) = 4 \cdot \frac{1}{2}\vec{E} \times \vec{H}$ where the factor of 4 is because in Fourier decomposition of time-dependent fields, only positive frequencies are

considered. We also only care about the cross-plane energy flow, and the flow is x-y coordinate independent, so

$$P(\omega, z_0) = Re(S_z(\omega, z_0)) = 4 \cdot \tfrac{1}{2} Re\left(E_x(z_0)H_y^*(z_0) - E_y(z_0)H_x^*(z_0)\right) \tag{2.66}$$

where * means the complex conjugate the field. Given fluctuation dissipation theorem equation, the Green's functions for E and H fields, and the Poynting vector equations above, the fields originating from both sides can be written as

$$\begin{aligned}
S_z(\omega, z_0) &= 2 \cdot \sum_{\alpha,\beta}\sum_{i,j}\left[i\omega\mu \int_{V_i} dV_i \bar{\bar{G}}^E_{x\alpha} \cdot \vec{J}_\alpha \left(\int_{V_j} dV_j \bar{\bar{G}}^H_{y\beta} \cdot \vec{J}_\beta\right)^* - i\omega\mu \int_{V_i} dV_i \bar{\bar{G}}^E_{y\alpha} \cdot \vec{J}_\alpha \left(\int_{V_j} dV_j \bar{\bar{G}}^H_{x\beta} \cdot \vec{J}_\beta\right)^*\right] \\
&= 2 \cdot 2 \cdot \sum_{\alpha,\beta} i\omega\mu [\int_{V'} dV' \bar{\bar{G}}^E_{x\alpha}(\vec{r}, \vec{r'}) \cdot \vec{J}_\alpha(\vec{r}) \left(\int_{V''} dV'' \bar{\bar{G}}^H_{y\beta}(\vec{r}, \vec{r''}) \cdot \vec{J}_\beta(\vec{r''})\right)^* - \dots \\
&\dots \int_{V'} dV' \bar{\bar{G}}^E_{y\alpha}(\vec{r}, \vec{r'}) \cdot \vec{J}_\alpha(\vec{r}) \left(\int_{V''} dV'' \bar{\bar{G}}^H_{x\beta}(\vec{r}, \vec{r''}) \cdot \vec{J}_\beta(\vec{r''})\right)^*] \\
&= \left[\int_{V'} dV' \int_{dV''} dV'' \delta(\vec{r'} - \vec{r''}) \left(\bar{\bar{G}}^E_{x\alpha}(\vec{r}, \vec{r'})(\bar{\bar{G}}^H_{y\alpha}(\vec{r}, \vec{r''}))^* - \bar{\bar{G}}^E_{y\alpha}(\vec{r}, \vec{r'})(\bar{\bar{G}}^H_{x\alpha}(\vec{r}, \vec{r''}))^*\right)\right] \\
&\times 2 \cdot 2 \cdot \sum_{\alpha,\beta} i\omega\mu\delta(\omega - \omega')\Theta(\omega, T)\frac{\epsilon_0\epsilon''\omega}{\pi} \\
&= \frac{1}{2} \times \left[\int_{V'} dV' (\left(\bar{\bar{G}}^E_{x\alpha}(\vec{r}, \vec{r'})(\bar{\bar{G}}^H_{y\alpha}(\vec{r}, \vec{r''}))^* - \bar{\bar{G}}^E_{y\alpha}(\vec{r}, \vec{r'})(\bar{\bar{G}}^H_{x\alpha}(\vec{r}, \vec{r''}))^*\right)\right] \\
&\times 2 \cdot 2 \cdot \sum_{\alpha,\beta} i\omega\mu\delta(\omega - \omega')\Theta(\omega, T)\frac{\epsilon_0\epsilon''\omega}{\pi}
\end{aligned}$$

where α β denotes x, y, z directions, and i, j denotes the different volumes that are integrated over, say i is the volume on the top and j is the volume on the bottom. The summation over i and j will give a factor of 2 too. If i and j are denoting different sources, then the cross terms in current should give us zero, meaning no correlation between two different sources. Thus only when i = j, the terms are nonzero. There are two identical sources, so there is a factor of 2 here. The factor of 1/2 after the third equal sign means that integrating the delta function over half-space gives the factor of 1/2.

Finally the power flow in the cross-plane direction is given as

$$P(\omega, z_0) = \frac{2\omega^2\epsilon_0\mu\Theta(\omega,T)}{\pi} Re\left(i\epsilon'' \int_{V'} dV' \left[G^E_{x,\alpha}(\vec{r}, \vec{r'}, \omega)G^{H^*}_{y,\alpha}(\vec{r}, \vec{r'}, \omega) - G^E_{y,\alpha}(\vec{r}, \vec{r'}, \omega)G^{H^*}_{x,\alpha}(\vec{r}, \vec{r'}, \omega)\right]\right) \tag{2.67}$$

Step 2: Further Simplifications

The Green's function found previously is given in terms of an integral over the parallel wave vectors, or a spatial Fourier transform. Thus, the power flow $P(\omega,z_0)$ can be further simplified as following

It was derived that

$$\bar{\bar{G}}(\vec{r}, \vec{r'}, \omega) = \int_{-\infty}^{+\infty} \frac{d\vec{k}_\parallel}{(2\pi)^2} \bar{\bar{g}}(\vec{k}_\parallel, z_0, z', \omega) e^{i\vec{k}_\parallel \cdot (\vec{R} - \vec{R'})} \tag{2.68}$$

where $\vec{R}=\hat{x}x+y\hat{y}$. Terms with e^{ikz} are left out to be dealt with later. All the terms with tick denotes a property of the source term, for example, $\vec{r}'$ is location of the source.

Plugging in the above expression leads to the equation

$$P(\omega, z_0) = \frac{2\omega^2\epsilon_0\mu\Theta(\omega,T)}{\pi} Re\left(i\epsilon'' \int_{-\infty}^{+\infty} \frac{d\vec{k}_\rho}{(2\pi)^2} \int_z dz' [g^E_{\rho\alpha} g^{H*}_{\theta\alpha} - g^E_{\theta\alpha} g^{H*}_{\rho\alpha}]\right)$$
$$= \frac{2\omega^2\epsilon_0\mu\Theta(\omega,T)}{\pi} Re\left(i\epsilon'' \times \frac{1}{2\pi} \int_0^{\infty} k_\rho dk_\rho \int_z dz' [g^E_{\rho\alpha} g^{H*}_{\theta\alpha} - g^E_{\theta\alpha} g^{H*}_{\rho\alpha}]\right)$$

where radial coordinates in k-space are used.

Step 3: Writing out Green's functions explicitly

The Green's function obtained in previous sections can be written out explicitly. Suppose the source is located in layer s at position z', and the point at which field is calculated is located in layer l at position z_c. The scalar Green's function g using Transfer Matrix Method (TMM) is given as

$$\bar{\bar{g}}^E_{sl} = \frac{i}{2k_{zs}} \begin{bmatrix} (A_l^{TE}\hat{e}(-k_{zl})\hat{e}(-k_{zl}) + A_l^{TM}\hat{h}(-k_{zl})\hat{h}(-k_{zl}))e^{i[k_{zl}(z_c-z_l)-k_{zs}z']} \\ + (B_l^{TE}\hat{e}(k_{zl})\hat{e}(-k_{zl}) + B_l^{TM}\hat{h}(-k_{zl})\hat{h}(k_{zl}))e^{-i[k_{zl}(z_c-z_l)-k_{zs}z']} \\ + (C_l^{TE}\hat{e}(-k_{zl})\hat{e}(k_{zl}) + C_l^{TM}\hat{h}(-k_{zl})\hat{h}(k_{zl}))e^{i[k_{zl}(z_c-z_l)+k_{zs}z']} \\ + (D_l^{TE}\hat{e}(k_{zl})\hat{e}(k_{zl}) + D_l^{TM}\hat{h}(k_{zl})\hat{h}(k_{zl}))e^{-i[k_{zl}(z_c-z_l)+k_{zs}z']} \end{bmatrix}$$

Green's function for magnetic field is found using $g^H_{sl}=\nabla\times g^E_{sl}$. Given definitions of unit vectors $\hat{e}(k_{z0})$ and $\hat{h}(k_{z0})$,

$$\nabla \times \hat{e}e^{ik} = i\hat{k} \times \hat{e}e^{ik} = -ik\hat{h}e^{ik}$$
$$\nabla \times \hat{h}e^{ik} = i\hat{k} \times \hat{h}e^{ik} = ik\hat{e}e^{ik} \qquad (2.69)$$

Therefore, the scalar Green's function for magnetic field can be written as

$$\bar{\bar{g}}^H_{sl} = \frac{k_l}{2k_{zs}} \begin{bmatrix} (A_l^{TE}\hat{h}(k_{zl})\hat{e}(-k_{zl}) - A_l^{TM}\hat{e}(k_{zl})\hat{h}(-k_{zl}))e^{i[k_{zl}(z_c-z_l)-k_{zs}z']} \\ + (B_l^{TE}\hat{h}(-k_{zl})\hat{e}(-k_{zl}) - B_l^{TM}\hat{e}(k_{zl})\hat{h}(k_{zl}))e^{-i[k_{zl}(z_c-z_l)-k_{zs}z']} \\ + (C_l^{TE}\hat{h}(k_{zl})\hat{e}(k_{zl}) - C_l^{TM}\hat{e}(k_{zl})\hat{h}(k_{zl}))e^{i[k_{zl}(z_c-z_l)+k_{zs}z']} \\ + (D_l^{TE}\hat{h}(-k_{zl})\hat{e}(k_{zl}) - D_l^{TM}\hat{e}(k_{zl})\hat{h}(k_{zl}))e^{-i[k_{zl}(z_c-z_l)+k_{zs}z']} \end{bmatrix}$$

(2.70)

Since in Step 2, the dyadic Green's function is expanded in space k_ϱ and in spatial coordinate z, the scalar Green's function can be expressed in the cylindrical coordinate

$$\hat{e}(k_{z0}) = \frac{1}{k_\rho}(\hat{x}k_y - \hat{y}k_x) = -\hat{\theta}$$

$$\hat{h}(k_{z0}) = \frac{1}{k_0}\hat{e}(k_{z0}) \times \vec{k}$$

(2.71)

Unit vectors $\hat{h}$ have both z and ϱ components. The unit vector $\hat{\Theta}$ don't couple with the other directions in the electric field. So the scalar Green's function written in matrix/tensor form is:

$$\overset{E}{g}_{sl} = \begin{vmatrix} \overset{E}{g}_{sl\varrho\varrho} & 0 & \overset{E}{g}_{sl\varrho z} \\ 0 & \overset{E}{g}_{sl\Theta\Theta} & 0 \\ \overset{E}{g}_{slz\varrho} & 0 & \overset{E}{g}_{slzz} \end{vmatrix} \tag{2.72}$$

Taking the $A_l^{TM}\hat{\rho}_l^+\hat{\rho}_s^+$ term as an example, the following is obtained

$$\begin{aligned} \frac{i}{2k_{zs}}\hat{\rho}_l^+\hat{\rho}_s^+ &= \frac{i}{2k_{zs}}\frac{1}{k_l}(k_\rho\hat{z} - k_{zl}\hat{\rho})\frac{1}{k_s}(k_\rho\hat{z} - k_{zs}\hat{\rho}) \\ &= \frac{1}{k_l k_s}\left(k_{zl}k_{zs}\hat{\rho}\hat{\rho} - k_{zl}k_\rho\hat{\rho}\hat{z} - k_{zs}k_\rho\hat{z}\hat{\rho} + k_\rho^2\hat{z}\hat{z}\right) \end{aligned}$$

Therefore terms in the Green's function tensor can be written out explicitly as

$$\bar{\bar{g}}^E_{sl\rho\rho} = \frac{ik_{zl}}{2k_s k_l}\begin{pmatrix} A_l^{TM}e^{i[k_{zl}(z_c - z_l) - k_{zs}z']} - B_l^{TM}e^{-i[k_{zl}(z_c - z_l) - k_{zs}z']} \\ -C_l^{TM}e^{i[k_{zl}(z_c - z_l) + k_{zs}z']} + D_l^{TM}e^{-i[k_{zl}(z_c - z_l) + k_{zs}z']} \end{pmatrix}$$

(2.73)

$$\bar{\bar{g}}^E_{sl\rho z} = \frac{ik_{zl}k_\rho}{2k_{zs}k_s k_l}\begin{pmatrix} -A_l^{TM}e^{i[k_{zl}(z_c - z_l) - k_{zs}z']} + B_l^{TM}e^{-i[k_{zl}(z_c - z_l) - k_{zs}z']} \\ -C_l^{TM}e^{i[k_{zl}(z_c - z_l) + k_{zs}z']} + D_l^{TM}e^{-i[k_{zl}(z_c - z_l) + k_{zs}z']} \end{pmatrix}$$

(2.74)

$$\bar{\bar{g}}^E_{sl\theta\theta} = \frac{i}{2k_{zs}}\begin{pmatrix} A_l^{TE}e^{i[k_{zl}(z_c - z_l) - k_{zs}z']} + B_l^{TE}e^{-i[k_{zl}(z_c - z_l) - k_{zs}z']} \\ +C_l^{TE}e^{i[k_{zl}(z_c - z_l) + k_{zs}z']} + D_l^{TE}e^{-i[k_{zl}(z_c - z_l) + k_{zs}z']} \end{pmatrix}$$

(2.75)

$$\bar{\bar{g}}^E_{slz\rho} = \frac{ik_\rho}{2k_s k_l}\begin{pmatrix} -A_l^{TM}e^{i[k_{zl}(z_c - z_l) - k_{zs}z']} - B_l^{TM}e^{-i[k_{zl}(z_c - z_l) - k_{zs}z']} \\ +C_l^{TM}e^{i[k_{zl}(z_c - z_l) + k_{zs}z']} + D_l^{TM}e^{-i[k_{zl}(z_c - z_l) + k_{zs}z']} \end{pmatrix}$$

(2.76)

$$\bar{\bar{g}}^{E}_{slzz} = \frac{ik_\rho^2}{2k_s k_l k_{zs}} \begin{pmatrix} A_l^{TM} e^{i[k_{zl}(z_c - z_l) - k_{zs} z']} + B_l^{TM} e^{-i[k_{zl}(z_c - z_l) - k_{zs} z']} \\ + C_l^{TM} e^{i[k_{zl}(z_c - z_l) + k_{zs} z']} + D_l^{TM} e^{-i[k_{zl}(z_c - z_l) + k_{zs} z']} \end{pmatrix}$$

(2.77)

Similarly,the scalar Green's function for magnetic fields can be written explicitly in tensor form.

$$\bar{\bar{g}}^{E}_{sl} = \begin{vmatrix} 0 & g^{H}_{slQ\Theta} & 0 \\ g^{H}_{sl\Theta Q} & 0 & g^{H}_{sl\Theta z} \\ 0 & g^{H}_{slzQ} & 0 \end{vmatrix} \tag{2.78}$$

$$\bar{\bar{g}}^{H}_{sl\rho\theta} = \frac{k_{zl}}{2k_{zs}} \begin{pmatrix} A_l^{TE} e^{i[k_{zl}(z_c - z_l) - k_{zs} z']} - B_l^{TE} e^{-i[k_{zl}(z_c - z_l) - k_{zs} z']} \\ + C_l^{TE} e^{i[k_{zl}(z_c - z_l) + k_{zs} z']} - D_l^{TE} e^{-i[k_{zl}(z_c - z_l) + k_{zs} z']} \end{pmatrix}$$

(2.79)

$$\bar{\bar{g}}^{H}_{sl\theta\rho} = \frac{k_l}{2k_s} \begin{pmatrix} - A_l^{TM} e^{i[k_{zl}(z_c - z_l) - k_{zs} z']} - B_l^{TM} e^{-i[k_{zl}(z_c - z_l) - k_{zs} z']} \\ + C_l^{TM} e^{i[k_{zl}(z_c - z_l) + k_{zs} z']} + D_l^{TM} e^{-i[k_{zl}(z_c - z_l) + k_{zs} z']} \end{pmatrix}$$

(2.80)

$$\bar{\bar{g}}^{H}_{sl\theta z} = \frac{k_l k_\rho}{2k_s k_{zs}} \begin{pmatrix} A_l^{TM} e^{i[k_{zl}(z_c - z_l) - k_{zs} z']} + B_l^{TM} e^{-i[k_{zl}(z_c - z_l) - k_{zs} z']} \\ + C_l^{TM} e^{i[k_{zl}(z_c - z_l) + k_{zs} z']} + D_l^{TM} e^{-i[k_{zl}(z_c - z_l) + k_{zs} z']} \end{pmatrix}$$

(2.81)

$$\bar{\bar{g}}^{H}_{slz\theta} = \frac{k_\rho}{2k_{zs}} \begin{pmatrix} - A_l^{TE} e^{i[k_{zl}(z_c - z_l) - k_{zs} z']} - B_l^{TE} e^{-i[k_{zl}(z_c - z_l) - k_{zs} z']} \\ - C_l^{TE} e^{i[k_{zl}(z_c - z_l) + k_{zs} z']} - D_l^{TE} e^{-i[k_{zl}(z_c - z_l) + k_{zs} z']} \end{pmatrix}$$

(2.82)

Given the scalar Green's functions, the power flow from sources in layer s to a location in layer l is given as

$$P(\omega, sl, z_0) = \frac{\omega^2 \epsilon_0 \mu \Theta(\omega, T)}{\pi^2} Re \left\{ i\epsilon'' \int_0^\infty k_\rho dk_\rho \int_{z_s}^{z_{s+1}} dz' \left[g^{E}_{sl\rho\rho} g^{H*}_{sl\theta\rho} + g^{E}_{sl\rho z} g^{H*}_{sl\theta z} - g^{E}_{sl\theta\theta} g^{H*}_{sl\rho\theta} \right] \right\}$$

where the integral over z specifies volume of the sources. For this thesis, the volume of sources should be a half-space.

Step 4: Finding field amplitudes using Scattering Matrix

From transfer matrix method, fields in layer 0 and layer 2 can be related by

$$\begin{bmatrix} A_0 \\ B_0 \end{bmatrix}$$

$$= V_{0,1} P_1 V_{1,2} \begin{bmatrix} A_2 \\ B_2 \end{bmatrix} = U_{0,2} \begin{bmatrix} A_2 \\ B_2 \end{bmatrix}$$

$$= \frac{1}{t_{0,1}} \begin{bmatrix} 1 & r_{0;1} \\ r_{0;1} & 1 \end{bmatrix} \begin{bmatrix} e^{-ik_{z1}(z_2-z_1)} & 0 \\ 0 & e^{ik_{z1}(z_2-z_1)} \end{bmatrix} \frac{1}{t_{1,2}} \begin{bmatrix} 1 & r_{1;2} \\ r_{1;2} & 1 \end{bmatrix} \begin{bmatrix} A_2 \\ B_2 \end{bmatrix}$$

where $r_{1,2}$ and $t_{1,2}$ denote Fresnel coefficients for reflection and transmission at the interface between layers 1 and 2. However, terms $e^{-ik_{z1}(z_2-z_1)}$ can become extremely large, when k_{z1} is imaginary; at the same time, terms $e^{ik_{z1}(z_2-z_1)}$ become really small. These would cause numerical errors and might not be solvable. The numerical instabilities become large for thick layers of materials, and for highly absorbing media.

To avoid this issue, the scattering matrix can be written as

$$\begin{bmatrix} A_l \\ B_0 \end{bmatrix} = S(0,l) \begin{bmatrix} A_0 \\ B_l \end{bmatrix} \tag{2.83}$$

Based on scattering matrix and transfer matrix, thus

$$U_{1,1}A_2 + U_{1,2}B_2 = A_1 = S(0,1)_{1,1}A_0 + S(0,1)_{1,2}B_1 = S(0,1)_{1,1}A_0 + S(0,1)_{1,2}(U_{2,1}A_2 + U_{2,2}B_2) \tag{2.84}$$

$$U_{2,2}B_2 + U_{2,1}A_2 = B_1 = \frac{1}{S(0,1)_{2,2}}B_0 + \frac{S(0,1)_{2,1}}{S(0,1)_{2,2}}A_0 \tag{2.85}$$

Writing in matrix form, it becomes

$$\begin{bmatrix} A_2 \\ B_0 \end{bmatrix} = S(0,2) \begin{bmatrix} A_0 \\ B_2 \end{bmatrix}$$

$$S_{1,1}(0,2) = \frac{S_{1,1}(0,1)t_{1,2}e^{ik_{z1}(z_2-z_1)}}{1-S_{1,2}(0,1)r_{1,2}e^{2ik_{z1}(z_2-z_1)}}$$

$$S_{1,2}(0,2) = \frac{S_{1,2}(0,1)e^{2ik_{z1}(z_2-z_1)}-r_{1,2}}{1-S_{1,2}(0,1)r_{1,2}e^{2ik_{z1}(z_2-z_1)}}$$

$$S_{2,1}(0,2) = \frac{S_{1,1}(0,1)S_{2,2}(0,1)r_{1,2}e^{ik_{z1}(z_2-z_1)}}{t_{1,2}} + S_{2,1}(0,1)$$

$$S_{2,2}(0,2) = \frac{S_{2,2}(0,1)[S_{1,2}(0,1)r_{1,2}+1]e^{ik_{z1}(z_2-z_1)}}{t_{1,2}}$$

For the parallel half-space configuration, S(0,2) is of interest. Assume that the source in in layer 0, and it is known that $B_2=0, A_0=e^{-ik_{z0}(z_1-z_0)}$. Given $A_2=S_{1,1}(0,2)A_0$ and above equations, S(0,1) and S(0,2) are calculated

$$S(0,1)=\begin{bmatrix} t_{01}e^{ik_{z0}(z_1-z_0)} & -r_{01} \\ \frac{r_{01}}{t_{01}}e^{ik_{z0}(z_1-z_0)} & \frac{e^{ik_{z0}(z_1-z_0)}}{t_{01}} \end{bmatrix} \tag{2.86}$$

$$A_2=S_{1,1}(0,2)A_0=\frac{t_{01}t_{12}e^{ik_{z1}(z_2-z_1)}}{1+r_{01}r_{12}e^{2ik_{z1}(z_2-z_1)}} \tag{2.87}$$

Step 5: Plugging in the Coefficients

In the current configuration, source is located in layer 0 and field reaches layer 2, so only the A coefficients in the Green's functions are accounted for. First listing out all the Green's functions and look at the z' dependence of the Green's functions.

$$\begin{aligned}
\bar{\bar{g}}^{E}_{02\rho\rho} &= A_2^{TM}e^{i[k_{z2}(z_c-z2)-k_{zs}z']}\frac{ik_{z2}}{2k_sk_2} \\
\bar{\bar{g}}^{H*}_{02\theta\rho} &= -A_2^{TM*}e^{-i[k^*_{z2}(z_c-z2)-k^*_{zs}z']}\frac{-ik^*_{z2}}{2k^*_sk^*_2} \\
\bar{\bar{g}}^{E}_{02\rho z} &= -A_2^{TM}e^{i[k_{z2}(z_c-z2)-k_{zs}z']}\frac{ik_{z2}k_\rho}{2k_{zs}k_sk_2} \\
\bar{\bar{g}}^{H*}_{02\theta z} &= A_2^{TM*}e^{-i[k^*_{z2}(z_c-z2)-k^*_{zs}z']}\frac{k^*_lk^*_\rho}{2k^*_sk^*_{zs}} \\
\bar{\bar{g}}^{E}_{02\theta\theta} &= A_2^{TE}e^{i[k_{z2}(z_c-z2)-k_{zs}z']}\frac{i}{2k_{zs}} \\
\bar{\bar{g}}^{H*}_{02\rho\theta} &= A_2^{TE*}e^{-i[k^*_{z2}(z_c-z2)-k^*_{zs}z']}\frac{k^*_{z2}}{2k^*_{zs}}
\end{aligned}$$

The z' term is always $e^{2k_{zs}''z'}$ where k_{zs}'' is the imaginary part of $k_{zs}=k_{zs}'+ik_{zs}''$. Taking the z' values from $-\infty$ to 0 gives the integral $\frac{1}{2k_{zs}''}$. An important assumption however is that $k_{zs}''>0$, or that the imaginary part of the k_z values is always chosen to be positive.

Therefore, writing out the total power transmitted from layer 0 to layer 2,

$$P_{02}(z_c=z_2)=\frac{\omega^2\epsilon_0\mu\Theta(\omega,T)}{2\pi^2}$$
$$Re\left(i\epsilon_0''\int_0^\infty k_\rho dk_\rho\frac{1}{k''_{zs}}\left[-\frac{ik_{z2}k_{2}^*}{4k_2|k_s|^2}|A_2^{TM}|^2-\frac{ik_{z2}k_2*|k_\rho|^2}{4k_2|k_s|^2|k_{zs}|^2}|A_2^{TM}|^2-\frac{ik_{z2}*}{4|k_{zs}|^2}|A_2^{TE}|^2\right]\right)$$

(2.88)

Two identities are important for simplifying the equation. Assume that k^2_{rho} which is the parallel wave vector is always real. Then,

$$\omega^2\varepsilon_0\mu\varepsilon_i''=2k_{zi}'k_{zi}''$$

$$k_{zi}'(|k_{zi}|^2+k_\rho^2)=\omega^2\varepsilon_0\mu Re(\varepsilon_i k_{zi}^*)$$

Both identities can be easily proved by algebraic expansion in real and imaginary space. Using these identities, after some algebraic manipulations, the power flow at $z=z_2$ is written as

$$P_{02}(z_c=z_2)=\frac{\Theta(\omega,T)}{4\pi^2}\int_0^\infty k_\rho dk_\rho \frac{1}{|k_{z0}|^2}\left[\frac{Re(\epsilon_0 k_{z0}^*)Re(\epsilon_2 k_{z2}^*)}{|n_0|^2|n_2|^2}\left|A_2^{TM}\right|^2+k_{z0}'k_{z2}'\left|A_2^{TE}\right|^2\right] \tag{2.89}$$

Step 6: Further Simplifications and Considering Sources from both Layer 0 and 2

This step involves a few important identities using which simplify the expression. Given

$$r_{12}^{TE}=\frac{n_1cos\theta_i-n_2cos\theta_t}{n_1cos\theta_i+n_2cos\theta_t}=\frac{k_{z1}-k_{z2}}{k_{z1}+k_{z2}}$$

$$r_{21}^{TE}=\frac{k_{z2}-k_{z1}}{k_{z1}+k_{z2}}=-r_{12}^{TE}$$

$$r_{12}^{TE}=\frac{n_2cos\theta_i-n_1cos\theta_t}{n_1cos\theta_t+n_2cos\theta_i}$$

$$r_{21}^{TE}=\frac{n_1cos\theta_t-n_2cos\theta_i}{n_1cos\theta_t+n_2cos\theta_i}=-r_{12}^{TE}$$

the identity $r_{12}=-r_{21}$ holds. Similarly, the identity $t_{21}=t_{12}\frac{k_{z2}}{k_{z1}}$ is true.

Two other identities used are

$$\frac{k_{zi}'}{|k_{zi}|^2}\left|t_{ij}^{TE}\right|^2=\frac{1}{|k_{zj}|^2}\left[k_{zj}'(1-\left|r_{ij}^{TE}\right|^2)-2k_{zj}''Im(r_{ij}^{TE})\right]$$

$$\frac{Re(\epsilon_i k_{zi}^*)}{|n_i|^2|k_{zi}|^2}\left|t_{ij}^{TM}\right|^2=\frac{1}{|k_{zj}|^2}\left[k_{zj}'(1-\left|r_{ij}^{TM}\right|^2)-2k_{zj}''Im(r_{ij}^{TM})\right]$$

(2.90)

which can be verified by plugging in the Fresnel coefficients and writing them in terms of complex k_z terms. The power transferred from a semi-infinite layer 0 that is incident at layer 2 can be written as,

$$P_{02}(z_c=z_2)=\frac{\Theta(\omega,T)}{4\pi^2}\int_0^\infty k_\rho dk_\rho\frac{1}{|k_{z0}|^2}\left[\frac{Re(\epsilon_0 k_{z0}^*)Re(\epsilon_2 k_{z2}^*)}{|n_0|^2|n_2|^2}\frac{\left|t_{01}^{TM}\right|^2\left|t_{21}^{TM}\right|^2\left|e^{ik_{z1}d}\right|^2}{\left|1-r_{10}^{TM}r_{12}^{TM}e^{2ik_{z1}d}\right|^2}\frac{|k_{z1}|^2}{|k_{z2}|^2}\right.$$
$$\left.+k_{z0}'k_{z2}'\frac{\left|t_{01}^{TM}\right|^2\left|t_{21}^{TM}\right|^2\left|e^{ik_{z1}d}\right|^2}{\left|1-r_{10}^{TM}r_{12}^{TM}e^{2ik_{z1}d}\right|^2}\frac{|k_{z1}|^2}{|k_{z2}|^2}\right]$$

$$P_{02}(z_c=z_2)=\frac{\Theta(\omega,T)}{4\pi^2}\int_0^\infty k_\rho dk_\rho\{(k_{z1}'(1-\left|r_{01}^{TE}\right|^2)-2k_{z1}''Im(r_{01}^{TE}))(k_{z1}'(1-\left|r_{21}^{TE}\right|^2)-2k_{z1}''Im(r_{21}^{TE}))$$
$$\frac{\left|e^{ik_{z1}d}\right|^2}{|k_{z1}|^2\left|1-r_{01}r_{12}e^{2ik_{z1}d}\right|^2}+(k_{z1}'(1-\left|r_{01}^{TM}\right|^2)-2k_{z1}''Im(r_{01}^{TM}))(k_{z1}'(1-\left|r_{21}^{TM}\right|^2)-2k_{z1}''Im(r_{21}^{TM})$$
$$\frac{\left|e^{ik_{z1}d}\right|^2}{|k_{z1}|^2\left|1-r_{01}r_{12}e^{2ik_{z1}d}\right|^2}\}$$

which can be simplified for propagating and evanescent waves. Propagating waves is defined as when $k_\varrho < k_0$ for k_0 is the wave vector in vacuum. In this case, $k_{z1} = k_{z1}' + i \times 0$. Vice versa, for evanescent waves when $k_\varrho > k_0$, $k_{z1} = 0 + i \times k_{z1}''$. The final version of the equation is given as

$$P_{02}(z_c = z_2)^{prop} = \frac{\Theta(\omega,T)}{4\pi^2} \int_0^{k_v} k_\rho dk_\rho \left[\frac{(1-|r_{10}^{TE}|^2)(1-|r_{12}^{TE}|^2)}{\left|1-r_{10}^{TE} r_{12}^{TE} e^{2ik_{z1}' d}\right|^2} + \frac{(1-|r_{10}^{TM}|^2)(1-|r_{12}^{TM}|^2)}{\left|1-r_{10}^{TM} r_{12}^{TM} e^{2ik_{z1}' d}\right|^2} \right] \tag{2.91}$$

$$P_{02}(z_c = z_2)^{evan} = \frac{\Theta(\omega,T)}{\pi^2} \int_{k_v}^{\infty} k_\rho dk_\rho e^{-2k_{z1}'' d} \left[\frac{Im(r_{10}^{TE}) Im(r_{12}^{TE})}{\left|1-r_{10}^{TE} r_{12}^{TE} e^{-2k_{z1}'' d}\right|^2} + \frac{Im(r_{10}^{TM}) Im(r_{12}^{TM})}{\left|1-r_{10}^{TM} r_{12}^{TM} e^{-2k_{z1}'' d}\right|^2} \right] \tag{2.92}$$

Integrands in above equation is the same if the subscripts 0 and 2 are switched, that is to say, the integrand for power flow from layer 2 to layer 1 is the same. The only difference is the term $\tau(\omega,T)$ which depends on temperature T. In summary, the net power flow is

$$\begin{aligned} P_{net,prop} &= P_{02}(z_c = z_2)^{prop} - P_{20}(z_c = z_0)^{prop} \\ &= \frac{\Theta(\omega,T_0) - \Theta(\omega,T_2)}{4\pi^2} \int_0^{k_v} k_\rho dk_\rho \left[\frac{(1-|r_{10}^{TE}|^2)(1-|r_{12}^{TE}|^2)}{\left|1-r_{10}^{TE} r_{12}^{TE} e^{2ik_{z1}' d}\right|^2} + \frac{(1-|r_{10}^{TM}|^2)(1-|r_{12}^{TM}|^2)}{\left|1-r_{10}^{TM} r_{12}^{TM} e^{2ik_{z1}' d}\right|^2} \right] \end{aligned} \tag{2.93}$$

Similarly for evanescent waves

$$\begin{aligned} P_{net,evan} &= P_{02}(z_c = z_2)^{evan} - P_{20}(z_c = z_0)^{evan} \\ &= \frac{\Theta(\omega,T_0) - \Theta(\omega,T_2)}{\pi^2} \int_{k_v}^{\infty} k_\rho dk_\rho e^{-2k_{z1}'' d} \left[\frac{Im(r_{10}^{TE}) Im(r_{12}^{TE})}{\left|1-r_{10}^{TE} r_{12}^{TE} e^{-2k_{z1}'' d}\right|^2} + \frac{Im(r_{10}^{TM}) Im(r_{12}^{TM})}{\left|1-r_{10}^{TM} r_{12}^{TM} e^{-2k_{z1}'' d}\right|^2} \right] \end{aligned} \tag{2.94}$$

These are the final equations for calculating near-field heat flux between two half-spaces, namely layer 0 and layer 2, with some material in layer 1. Rest of the thesis will rely heavily on these two equations.

Chapter 3

Ferroelectrics

In this chapter, the author first explains the phase change behaviors for ferroelectric materials, both macroscopically and microscopically. General models to describe tunable dielectric dispersion of ferroelectric materials is introduced. These models are later used in Chapter 4. At the end of the chapter, a brief introduction to several competing theories of ferroelectrics is included with references.

1 Phase Change and Temperature Dependence of Material Properties

Phase change of a crystal means that structure of the material changes from structure A to structure B. In displacive-type ferroelectric materials, the change is usually from rhombohedral structure of a ferroelectric material to a tetragonal structure, which makes the material paraelectric. The ferroelectric phase is generally defined as the phase with inherent dipoles, while the paraelectric phase does not have inherent dipoles. The tetragonal (paraelectric) phase is symmetric in terms of + and - charged ions, and thus there exists no inherent dipole or spontaneous polarization. Yet in rhombohedral (ferroelectric) case, due to displacement of center atoms relative to the "cage" atoms, there exists inherent dipole within the structure. As will be mentioned later, another property of ferroelectric to paraelectric phase transition is that, in ferroelectric phase dielectric constant increases with temperature until it reaches Curie temperature and transitions to paraelectric phase; after the material changes to paraelectric phase, dielectric constant drops with temperature.

Classical theories of chemistry and physics dictate that materials tend to stay in lowest free-energy state where free energy F is given by $F=U-TS$. For a structure to phase change as temperature varies, the following requirement has to satisfy

$$F_A(T_c)=F_B(T_c) \tag{3.1}$$

The internal energy U and entropy S depends on the material structure. For example, since different structures have different phonon/electron dispersions, entropy of different structures are also different. Suppose structure B have lower-frequency phonon bands, usually denoted as "softer" phonons, than structure A, then more phonons are excited in structure B at the same temperature. This leads to $S_B>S_A$ at the same temperature T [48]. Assuming a nearly constant internal energy U, larger entropy in structure B lowers the free energy U and thus the material transitions into structure B. This is exactly what happens in some ferroelectrics.

As an exmaple, one can look at the phonon dispersion of $SrTiO_3$ [53]. At transition temperature T_c, the first transverse optical mode reaches zero, which corresponds to infinite dielectric constant. Here, since T_c is around 40K[53], both measurements show $SrTiO_3$ in the paraelectric phase. The phonon frequency slowly softens as temperature reduces from 293K to 90K near zone-center, toward the zero-value. Soft phonons only occur for small wave vectors close to zone center. In SrTiO3, actually zone-boundary acoustic phonons also show considerable amount of softening. This is not a ferroelectric transition, but the author will not go into details here.

One can usually classify ferroelectric phase transitions as displacive type or order-disorder type. The theories and descriptions following apply primarily to displacive type.. As briefly mentioned, typical structure of displacive-type ferroelectrics is the perovskite structure ABO_3. Perovskite structures typically have properties highly dependent on external factors, such as polarization, magnetic field, strain and temperatur. and is unique in many ways. The following paragraphs will explain why phase change with temperature happens in ferroelectrics, both macroscopically and microscopically.

Microscopically, temperature changes the lattice spacing by thermal expansion, breaking the balance between ionic forces and short-range atom interaction forces. As a result, the center ion, namely the B atom in ABO_3, displaces from its equilibrium. This changes the local fields of polarization within the unit cell, which in turn changes the macroscopic dielectric properties. From Clausius-Mossotti relation,

$$\varepsilon = \frac{1+\frac{8\pi\alpha}{3v}}{1-\frac{4\pi\alpha}{3v}} \tag{3.2}$$

where α is the sum of ion polarizations in the primitive cell, and v is the column of primitive cell. The dielectric constant becomes infinite when $\frac{4\pi\alpha}{3v}=1$.

In ferroelectrics, the temperature when phase change happens is the Curie temperature T_c. This is the temperature when $\frac{4\pi\alpha}{3v}=1$. Since changing temperature changes volume of the unit cell, and if we assume that

$$\frac{4\pi\alpha}{3v}=1-3s \tag{3.3}$$

then one can derive that dielectric constant is inversely proportional to the difference between current temperature and Curie temperature[48]

$$s = \frac{(T - T_c)}{K} \tag{3.4}$$

$$\varepsilon = \frac{K}{T - T_c} \tag{3.5}$$

where usually s is linearly proportional to temperature only close to the Curie temperature.

Another important phenomena is TO-mode condensation, or that TO mode becomes zero-frequency at Curie temperature. From Lyddane-Sachs-Teller relation $\frac{\omega_{TO}^2}{\omega_{LO}^2} = \frac{\varepsilon(\infty)}{\varepsilon(0)}$, this is immediately obvious.

3 Soft Mode Tunability with Temperature and Electric Field

In addition to temperature dependent properties, ferroelectrics also show dependence on applied electric field. This dependence is usually much smaller than that on the temperature. Physically, the electric field dependence of material properties is also due to displacement of atoms and how it changes the total polarizability within primitive cell. Atoms are oppositely charged in the primitive cell, so external electric field would displace charged atoms relative to each other, changing the value $\frac{\alpha}{v}$ where α is total polarizability of ionic pairs and v is the volumn of a primitive cell.

In general, Landau theory is used to describe how the material property changes with electric field. Whether the phase transition is continuous as in second-order phase transitions, or discontinuous as in first-order phase transitions, the Landau theory gives good theoretical explanations. The free energy of the crystal is written as [48]

$$F(P,T) = -EP + g_0 + \frac{1}{2}g_2P^2 + \frac{1}{4}g_4P^4 + \frac{1}{6}g_6P^6 + \ldots. \tag{3.6}$$

where the g coefficients depend on temperature, E is the external field, and P is the polarization within the crystal. At equilibrium, the free energy is minimum, and $dF/dP = 0 = -E + g_2P + g_4P^3 + g_6P^5 + \ldots..$ In addition, the term g_2 depends on temperature, and we assume that $g_2 = K(T - T_0)$. Substiting these two equations into Eq. (3.6), one obtains an equation that relates external electric field to the internal polarizations P inside the material.

In second-order phase transitions, the term g_4 is positive, and thus

$$E = K(T - T_0)P + g_4P^3 \tag{3.7}$$

In first-order phase transitions, the term g_4 is negative and thus

$$E=K(T-T_0)P- \left|g_4\right|P^3+g_6P^5 \tag{3.8}$$

Assuming in general that P^3 and P^5 terms is small, then from $\varepsilon=1+4\pi P/E$, one gets $\varepsilon=1+4\pi \frac{1}{K(T-T_0)}$ as shown before. If we cannot neglect the high-order P terms, the dielectric constant can be written as

$$\begin{aligned}\frac{1}{\epsilon} &= \frac{1}{1+4\pi\frac{P}{E}} \\ &\approx \frac{E}{4\pi P} \\ &= \frac{K(T-T_0)+g_4P^2+g_6P^4}{4\pi}\end{aligned} \tag{3.9}$$

where one assumes that $4\pi P/E \gg 1$. The assumption is usually valid since ferroelectrics have large dielectric constants. From Eq. (3.9) above, the dielectric is inversely proportional to a 4th power polynomial in P. In fitting with real materials, we assume that the inverse dielectric constant $1/\varepsilon$ is quadratic with external electric field for simplicity.

The effects of electric field on ferroelectric soft modes were first measured by Fleury[54, 55]. One can indeed show that squared soft phonon frequency can be changed via electric field and temperature.

4 Dielectric Response

The dielectric response of ferroelectric materials over frequency can be described as multiple Lorentz oscillators coupled with a Debye relaxor. Debye relaxor behavior of ferroelectrics typically occur at low frequencies, and describes how the population of dipoles within the ferroelectric material interact with each other and how they respond to external electric field [57]. Lorentz oscillator describes a more narrow-band response near the transverse and longitudinal optical phonon frequencies as described in Chapter 2. In real ferroelectric materials, the Debye mode and Lorentz mode can couple, so the coupled mode theory is used to describe the dielectric dispersion [56]

$$\epsilon_{Lorentz}(\omega) = \frac{f}{\omega_0^2 - \omega^2 - i\omega\tau}$$
$$\epsilon_{Debye}(\omega) = \frac{g}{1 - i\frac{\omega}{\gamma}}$$
$$\epsilon_{Coupled}(\omega) = \frac{f(1 - i\omega/\gamma) + g(\omega_0^2 - \omega^2 - i\omega\tau) + 2\delta\sqrt{fg}}{(\omega_0^2 - \omega^2 - i\omega\tau)(1 - i\omega/\gamma) - \delta^2}$$

(3.10)

where δ describes the coupling strength.

The coupled mode theory deals with systematic response in which non-negligible coupling exists between two modes. One can write the Green's function **G**(ω) for the material dielectric response as [56]

$$G^{-1}(\omega) = \begin{vmatrix} 1-i\omega/\gamma & \delta \\ \delta & \omega_0^2-\omega^2-i\gamma \end{vmatrix} \quad (3.11)$$

Suppose the strength of modes is given by $S=(g^{1/2}, f^{1/2})$, then the dielectric function is given by $\varepsilon(\omega)= \sum_{i,j} S_i S_j G_{ij}(\omega)+\varepsilon_\infty$. After algebra manipulations, the coupled mode equation for dielectric constant is obtained.

According to phase-change theory described in previous sections, the following assumptions are made

- Lorentz oscillator frequency squared ω_0^2 is proportional to inverse dielectric constant, which is a quadratic equation of external field E. This relation is further simplified to be $\omega_0=C\cdot E$

- Similarly, ω_0^2 is proportional to inverse dielectric constant, which is a linear function of T near curie temperature, but can be better approximated as a quadratic function of temperature T in the entire temperature range;

- Relaxor strength g is a quadratic function of temperature T as well. This is because in general, dielectric constant of relaxor ferroelectrics increases with temperature first and then drops [59] and needs to be described by a second-order polynomial. The quadratic function is picked because it's simple, but still captures the general trend.

- All other parameters are assumed constant with temperature T and external field E.

Based on the above assumptions, we write

$$\omega_0=C_E E+log\left(\frac{-e^{C_{T0}+C_{T1}T+C_{T2}T^2}}{2}\right) \quad (3.12)$$

$$g=K_{T0}+K_{T1}T+K_{T2}T^2 \tag{3.13}$$

5 Origins of Instability: Several Theories and Numerical Computations

Several theories were developed to describe soft mode hardening or softening behavior in ferroelectrics for a few decades. In addition to Landau theory described above where free energy equation is crucial, other microscopic frameworks are (1) electron-phonon scattering; (2) anharmonic scattering between phonon modes [61]; (3) disorder-order phase transition for relaxor ferroelectrics especially[62].

Electron-phonon scattering uses quantum mechanics, primarily scattering theory and Fermi's golden rule, to describe how the lattice interacts with dipoles within the crystal. This is one of the most widely used theories to describe electric-field dependence of soft-modes. Cowley first proposed that temperature dependence for TO mode comes from the anharmonic interaction between all phonon modes[61]. And disorder-order phase transition theory is most widely used for relaxor ferroelectrics.

Due to advances in first-principles calculations, many have tried to calculate material properties of ferroelectrics. However, since first-principles calculations typically only deal with T = 0K calculations, phase transition phenomena are not best captured. To describe the soft phonon effects using electric field, the referenced papers [64] usually apply an external electric field in the simulation cell and calculates the soft-phonon frequency.

Chapter 4

Simulation Results

1 Dielectric Response of Ferroelectrics

The dielectric response of ferroelectrics is described before as coupled Lorentz oscillator and Debye relaxation, a combination of ionic and dipole response. Due to lack of experimental data, we use the experimental fitting procedure followed in this paper [56] to obtain the following parameters.

The material simulated is SrTiO3/DyScO3 superlattice structure where each layer is 50nm thick. The transition temperature is determined to be between 275K and 300K [56]. One important thing to note that the numerical values of frequencies are relevant in unit of 1/cm. The electric fields have unit kV/cm. The temperatures have units K. The unit of C_E is 1/kV.

Parameter	Related Equations	Descriptions
ω_0	$\omega_0 = C_E E + \log\left(\frac{-e^{C_{T0}+C_{T1}T+C_{T2}T^2}}{2}\right)$	Transverse optical phonon frequency changes
g	$g = K_{T0} + K_{T1}T + K_{T2}T^2$	Strength of Debye Relaxor
f,γ,τ,δ	$\varepsilon_{Coupled}(\omega) = \frac{f(1-i\omega/\gamma)+g(\omega_0^2-\omega^2-i\omega\tau)+2\delta\sqrt{fg}}{(\omega_0^2-\omega^2-i\omega\tau)(1-i\omega/\gamma)-\delta^2}$	Coupled Dielectric Response

Table 4.1: List of Fitting Parameters for Dielectric Response

Parameter	Numerical Value
C_E	0.2655
C_{T0}	6.9965×10^{-5}
C_{T1}	7.9085×10^{-7}
C_{T2}	2.1220×10^{-9}
K_{T0}	284.2753
K_{T1}	-1.2225
K_{T2}	8.1647×10^{-4}
f	2.17×10^{6}
γ	8.4458
τ	46.6263
δ	32.8994

Table 4.2: Values for Fitting Parameters for Dielectric Response

The fitted curves are plotted with experimental data from paper by Kadlec et al. to see how well the curves fit. Although fitting for the curves do not show complete agreement, the fitting curves capture the general shape of dispersion relation and the general trend when one varies temperature and electric field.

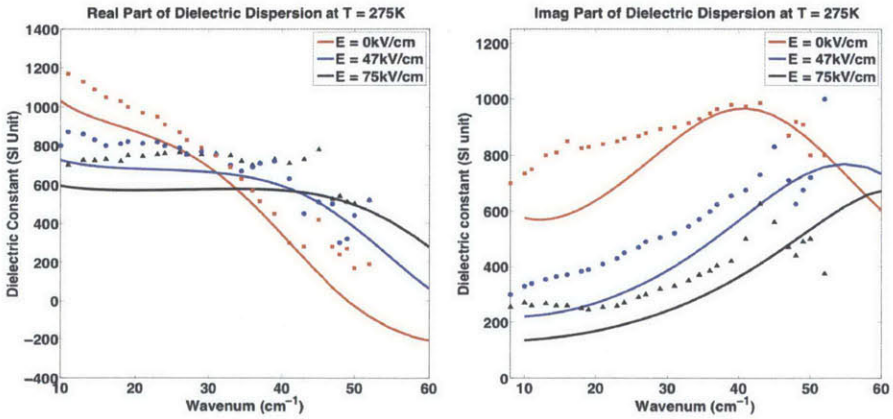

Figure 4.1: Fitted dielectric dispersion at T = 275K with experimental data from Kadlec et al. [56] plotted as data points.

To better grasp the meaning of these parameters, the author plots how squared transverse optical (TO) phonon frequency changes with temperature T and electric field E in Figure 4.2. To see the effect on Debye response, several responses at various temperatures are plotted as well. As shown in Figure 4.2, the uncoupled Debye response at low frequencies drops as temperature

increases, because its strength g drops as temperature increases. However, as will be seen in Figure 4.2, the effect is reversed by Lorentz response. Dielectric constant at low frequencies increases as temperature increases.

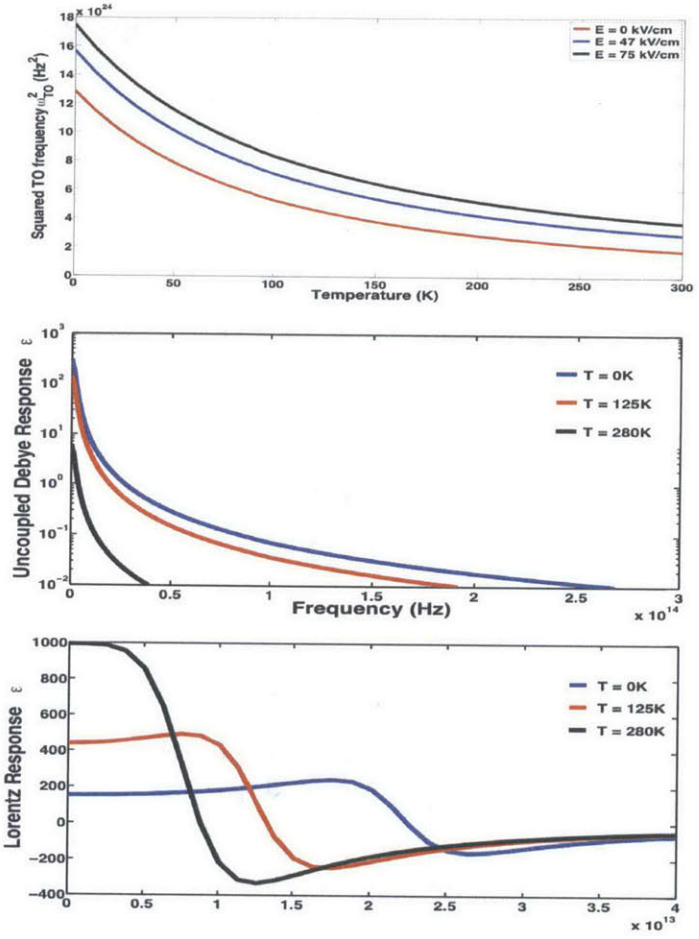

Figure 4.2: Top: Squared TO Frequency ω_{TO}^2 vs. Temperature for Different Electric Fields; Middle: Uncoupled Debye Response at Various Temperature; Bottom: Uncoupled Lorentz Response at Various Temperatures

As shown in Figure 4.2(b), TO phonon softens as temperature increases. This is because the TO phonons can behave differently in thin films due to other effects such as the additional stress generated from epitaxial growth on the substrate. The source for experimental data also comments that the material is still within ferroelectric phase. The author does not comment further on the matter.

Plugging in the fitting parameters in, in Figure 4.3, the following typical dielectric response is observed with a low frequency Debye relaxation response and a higher frequency Lorentz response. Low frequency Debye relaxation response corresponds to dipole contribution to

dielectric constant, while the higher frequency corresponds to ion contribution, which in turn relates to TO and LO phonon frequencies.

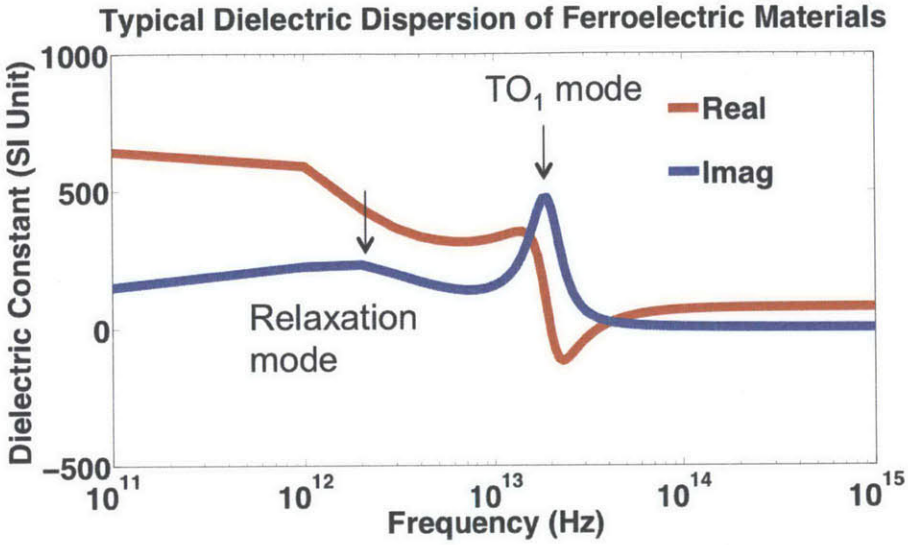

Figure 4.3: Typical Dielectric Response of Ferroelectric Material

As temperature increases, the TO phonon frequency ω_0 decreases, meaning that the dielectric constant increases with temperature. The material is within the ferroelectric phase. How the dielectric response changes with temperature is observable in Figure 4.4. As electric field increases, the TO phonon frequency ω_0 increases, meaning that the dielectric constant decreases with electric field E. How the dielectric response changes with electric field is also observable in Figure 4.4.

Landau theory can be used to describe why increasing electric field drops TO phonon frequency. In Chapter 3, it was derived that

$$\begin{aligned}\frac{1}{\epsilon} &= \frac{1}{1+4\pi\frac{P}{E}} \\ &\approx \frac{E}{4\pi P} \\ &= \frac{K(T-T_0)+g_4P^2+g_6P^4}{4\pi}\end{aligned}$$

(4.1)

If g_4>0, then inverse dielectric constant 1/ε increases with electric field E and P, and so does the TO frequency.

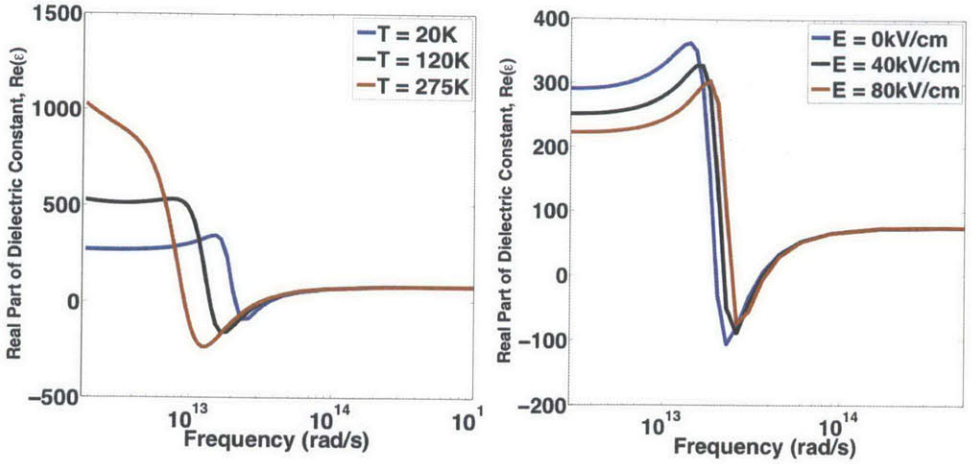

Figure 4.4: Dielectric Response with Changing Temperature and Changing Electric Field

Some fitting parameters and procedures chosen are empirical, nevertheless the equations give a good fit with experimental results. It might be worthwhile to note that the material referred is a superlattice of 50nm SrTiO3 grown on 50nm of DyScO3. Phonon mean free path in many materials are larger than 50nm, so phonons behave different in a superlattice from a bulk material. However, how this affects the dielectric response of the material is largely unexplored. One can refer to the reference[56] to look for more details on the material.

2 Spectral Heat Transfer vs. Electric Field

The set up of interest in this thesis is: hot side temperature is at 80K and cold side temperature is at 20K. Although the temperatures are at cryogenic temperatures, the mechanism of tuning spectral heat flux is all the same at higher temperatures. This 20K-80K configuration is chosen because the largest contrast in heat flux tuned **only** by electric field is observed, which is primarily because the surface phonon polariton mode lies around 50um. Radiation at 50um is best excited at 60K according to Wien's displacement law. Transition temperature actually does not play that big a role here; transition temperature for this material is around room temperature. At different temperatures, as in Figure 4.2(b), tunability by electric field (difference between max and min TO frequency) does not change much at different temperatures, curves are rather parallel.

The distance between hot and cold side is kept at 100nm as an example. As shown previously, the hot side automatically shows a lower frequency phonon polariton mode than cold side. Increasing electric field on the hot side would pull surface phonon polariton modes closer, thus increasing heat flux. Vice versa, increasing electric field on cold side would pull modes farther apart, decreasing heat flux. The change in spectral heat flux is observed in Figure 4.5.

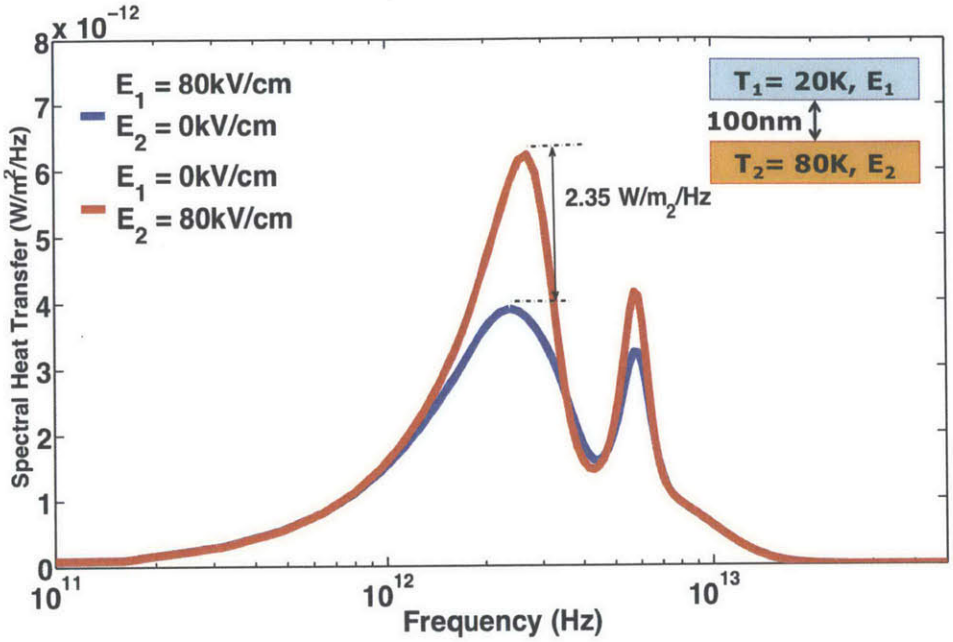

Figure 4.5: Spectral Heat Flux with Changing Electric Field

Additionally, increasing electric fields on both sides increases the TO phonon frequencies on both sides, by about the same amount. Thus the spectral heat flux should also show a shift to higher frequencies. This is indeed the case.

The results here are central to the tuning mechanism of spectral heat flux. As described in Chapter 4, the proposed mechanism of this thesis takes advantage of two mechanisms. First mechanism is the strength of coupling of surface phonon polariton modes from opposing surfaces. The result of that coupling directly affects the amount of heat transferred, as evident in Figure 4.5. Second major mechanism is by changing the material parameters directly. Of course coupling of surface modes also plays a role in transferring heat across the gap, but as seen in Figure 4.6, the primary source of heat transfer change is the shift in TO frequency.

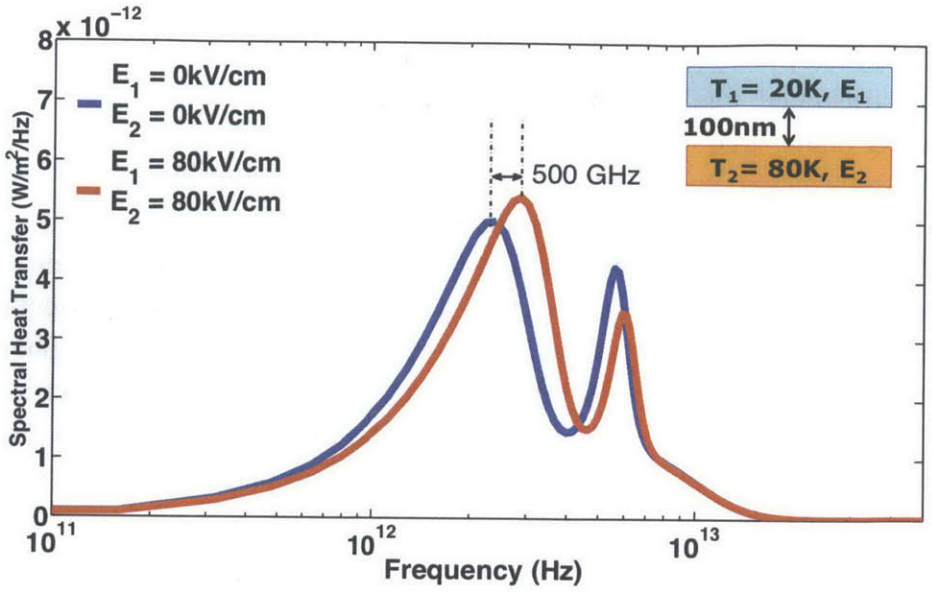

Figure 4.6: Spectral Heat Flux with Changing Electric Field

3 Spectral Heat Transfer vs. Temperature

A larger change in TO phonon frequency is obtainable by changing temperature, as larger phase change effects are shown. Therefore by changing temperature, spectral heat flux not only increased in magnitudes but is also shifted by a large amount. This is indeed observable as configuration temperatures are changed from 20K-80K to 290K-320K around room temperature.

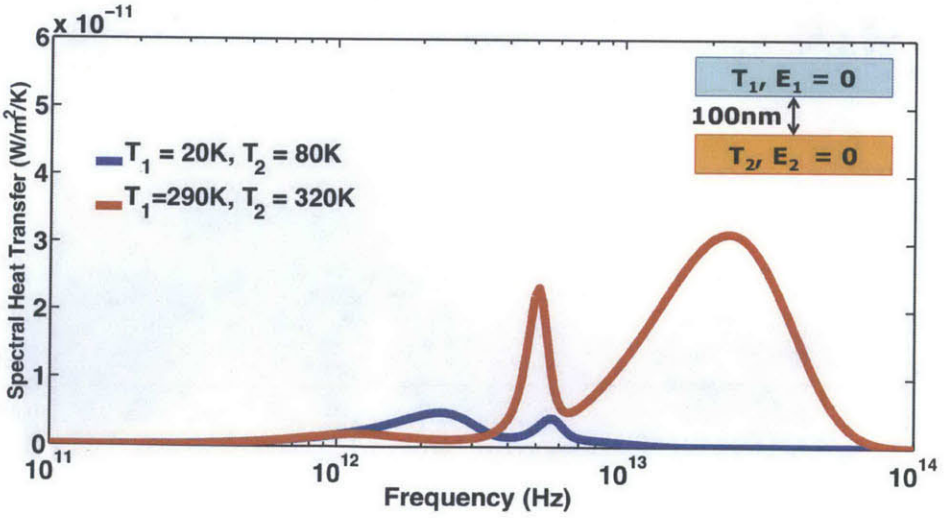

Figure 4.7: Spectral Heat Flux with Changing Temperature

There are 3 observable peaks instead of 2 at higher temperatures. The first two peaks correspond to surface phonon polariton modes. The 3rd large peak around 2~3 $\times 10^{14}$ Hz is excited due to frustrated total internal reflection. It is best observable in the transmission function. Exciting higher-frequency modes requires larger energy, and thus higher temperatures. The dominant frequency range excited is described best by the difference between energy distribution functions of photons at temperature T_1 and T_2.

The readers might notice that surface phonon polariton frequencies do not decrease necessarily with temperature. For example, the 2nd surface phonon polariton frequency increase with increasing temperature, while the 1st decreases. This is because surface phonon polariton frequencies as described in Chapter 1 corresponds to when the material dielectric constants on both sides of the interfere sum up to 1. Although surface phonon polaritons often happen near Lorentz response of the material, it does not correspond one-to-one to the TO phonon frequency.

However, this large shift in spectral heat flux can be advantageous in various settings, for example, for temperature sensor or other devices tunable by temperature changes.

4 Transmission Function and Dispersion Relation

The transmission function can be used to explain how spectral heat flux changes with temperature. The transmission function shows the number of available modes through which heat can be transferred. However, which modes are excited is determined by temperature. Temperature indicates excitation energy $\approx 3/2 k_B T$, then modes at frequencies typically lower than this energy can be excited. The transmission function between materials at 20K-80K configuration without electric field is shown in Figure 4.8. For example, at room temperature, the peak excitation energy is around 40×10^{12} rad/s. nal

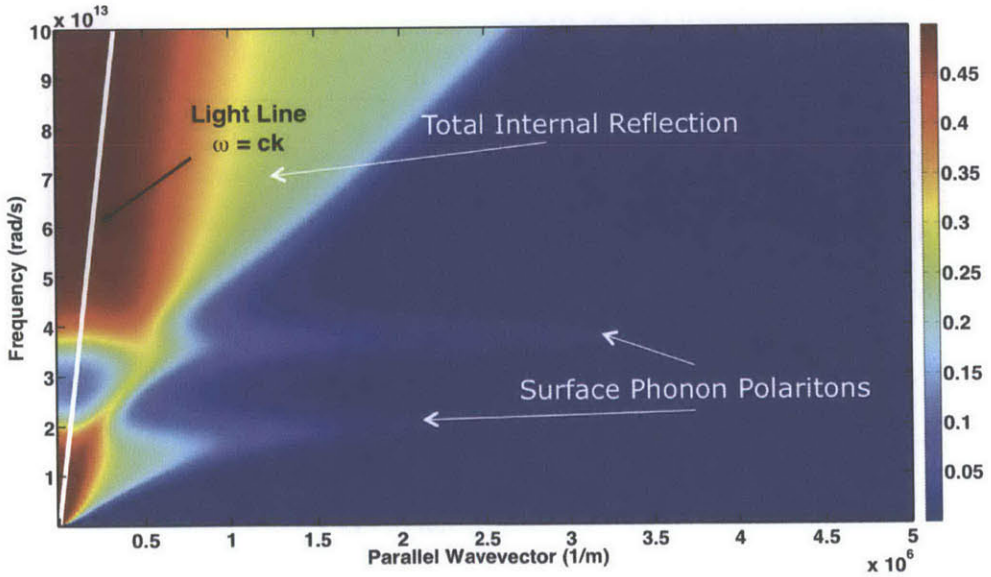

Figure 4.8: Transmission Function at 20K-80K configuration with 100nm separation

5 Total Heat Flux Tunability

The total heat flux can be integrated from above calculations. For the 20K-80K configuration, suppose just the electric field is modified. The largest increase in heat flux is around 15%. The largest electric field selected is 80kV/cm as suggested [56] as the break-down electric field of the material. What is important to note is that there is no maximum limit for the total heat flux as we change electric field. The primary practical limitation is the break-down electric field.

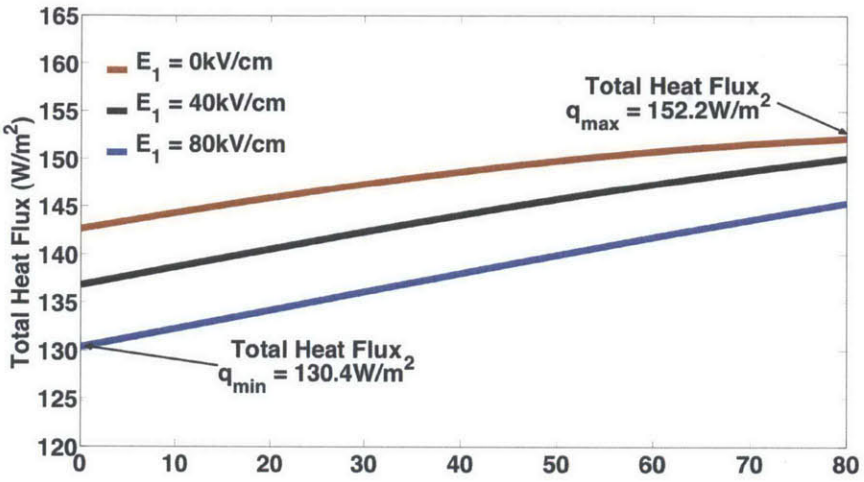

Figure 4.9: Total Heat Flux with Changing Electric Field

In looking for the maximum total heat flux change using electric field only, the maximum and minimum heat flux at each temperature is calculated. For example, the calculation is performed by fixing temperature at 100K and 200K, and sweeping the electric field values applied on both sides from 0 to 80kV/cm. The maximum heat flux is q_{max} found at some electric field values $E_{1,max}$ and $E_{2,max}$, while the minimum heat flux q_{min} is found at $E_{1,min}$ and $E_{2,min}$. Then the tunability is calculated to be $\frac{q_{max}-q_{min}}{q_{min}}\times 100\%$.

The tunability values are plotted on a contour plot for different temperatures. The maximum tenability is indeed around 15% at 20K-80K configuration.

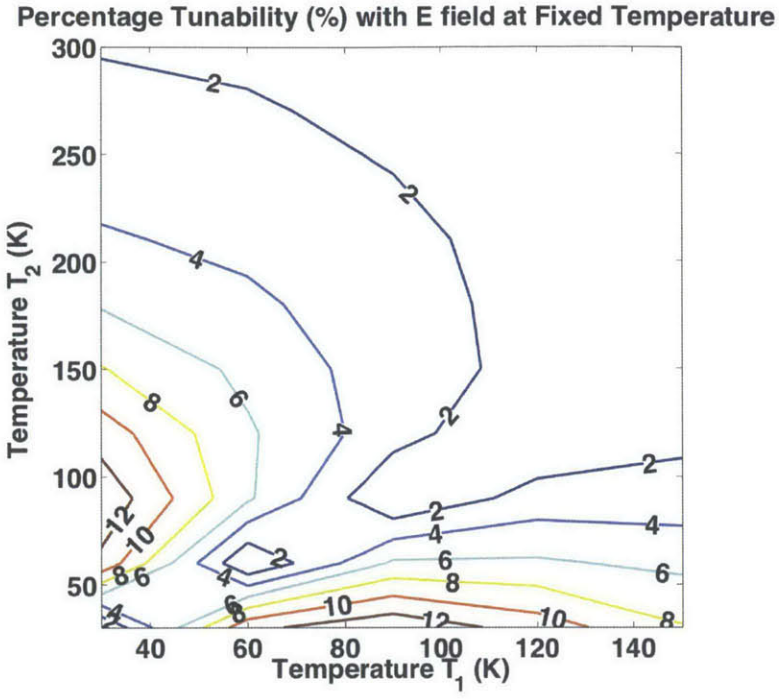

Figure 4.10: Tunability of Total Heat Flux at Different Temperatures

6 Enhancement over Blackbody

Another important factor to look at is how much enhancement over blackbody is achievable. One primary advantage for near-field heat transfer is the much larger heat flux in the near-field regime than far-field regime. Therefore, it is advantageous for large heat flux applications. The enhancement over blackbody comes from two major mechanisms: (1) Surface phonon polariton modes; (2) Total Internal Reflection. The effects of total internal reflection is generally felt at larger distances from the surface, due to its larger decay length than surface phonon polariton modes.

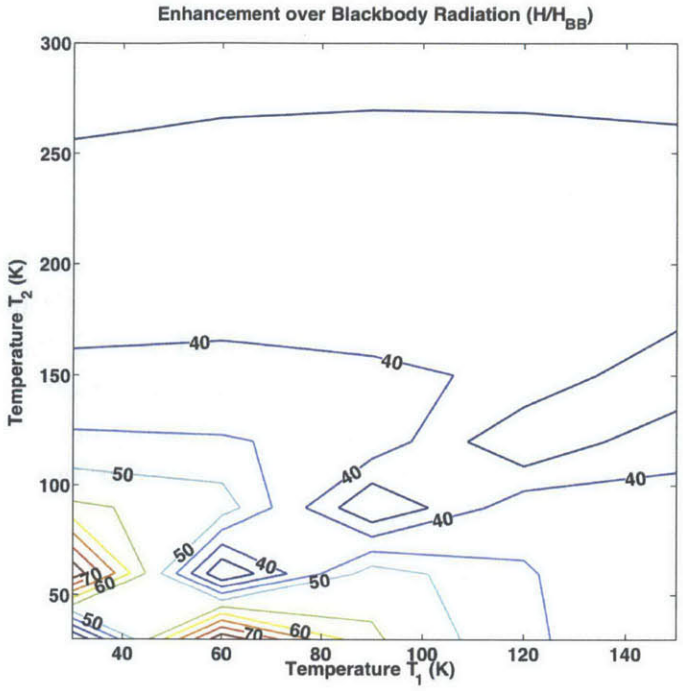

Figure 4.11: Enhancement of Total Heat Flux over Blackbody at Different Temperatures

The largest enhancement over blackbody is at 30K-60K configuration. At this temperature, the device best outperforms far-field radiative transfer.

Chapter 5

Conclusions and Future Work

Based on relevant theories in Chapter 2 and 3, the author has shown in Chapter 4 that the total heat flux can be changed by as much as 15% by changing electric field only when hot side and cold side are kept at 80K, 20K respectively. The distance is kept at 100nm. Both the magnitude and frequency of spectral heat flux can be changed via applying electric field. It is also shown that the largest tenability by electric field **only**, without changing other parameters, happens at 20K-80K configuration. Temperature also changes the spectral heat flux significantly by including higher-frequency totally internal reflected modes.

As proposed in Chapter 1, this work can be used potentially in three of the major applications for near-field heat transfer, namely thermal emitter, TPV cells and electronics cooling.

1 Other Control Mechanisms

As discussed previously, there are generally two ways in which to control heat transfer in near-field radiation. The first and more widely used method is by looking at interesting materials. The second mechanism is catching the trend now, that is by proposing interesting configurations/geometries of opposing materials. For example, Ben-Abdallah [35] discussed a sandwich structure with a third material acting as "gate" in a thermal transistor. The mechanism primarily used in this thesis also falls in this category. Another mechanism can be using thickness of the emitter and receiver to introduce wave guided modes into the transmission function, changing the transmission characteristics[66].

2 What happens near phase transition?

Another path worth exploring for tunable heat-flux in current thesis is to focus on near-phase-transition temperatures. As evident in chapter 3, the largest dielectric constant contrast happens near the phase transition temperature. The current material system investigated is a thin-film ferroelectric superlattice with phase transition temperature around 280K.

However, since phonon polaritons are not excited near phase transition temperature, we can not take advantage of the large change in the transverse optical (TO) phonon frequency. Therefore, the evident follow-up to the proposed mechanism is to explore ferroelectric-like phase-change materials with both of the following properties:

- TO phonon frequency falls around 10um for room-temperature applications;
- Phase transition temperature is close to desired operating temperature.

A quick search in literature shows that typical bulk ferroelectric materials have TO phonon frequency ω_{TO} less than 10THz. 10um wavelength correspond to a 30THz frequency. The phase transition temperature can be controlled by thin-film configurations or epitaxial growth of materials on lattice-matched substrates, so the major challenge is to find a material with high TO frequency. In general, that means lighter atoms with stronger force constants.

3 Crystal lattice and Sub-wavelength control of Radiation

Another largely unexplored path in tunable heat flux is by modifying crystal lattice. The first paper using such control is a 2006 paper [67] by Ocelic et al. published on Nature. The authors impinged the SiC lattice using carbon ions and implanted a check board pattern. The observed radiation pattern shows a contrast in amount radiated, specifically following check board patterns. The decrease in radiation is in part caused by crystal lattice defects, which makes SiC amorphous and thus does not support surface phonon polariton modes.

Similar behaviors is being explored in the field of defect engineering. By changing the position and amount of defects in fuel cells, diamonds or other materials change the material properties such as dielectric constant, reactivity with chemicals, or thermal conductivity [68]. In ferroelectric materials, a number of sub-wavelength phenomena can be used to control surface phonon polaritons locally. A quick literature search validates that for low-frequency dielectric response, or the Debye relaxation behavior, oxygen-vacancy is an important parameter. However, there is no indication that oxygen vacancy actually creates enough perturbation as a "defect" to change dielectric behaviors in IR range.

Ferroelectrics also have domains in which polarizations can be switched on/off and reversed directions. Direction of dipoles within a ferroelectric means the direction in which oxygen atoms are displaced. Center atoms displacing in different directions usually means a large change in dielectric constant, as well as its local crystal structure. This may allow another dimension of tunability for the proposed device. In the literature, there also has been studies on how domain wall motion affect permittivity of the material [70] in the kHz range. However, the effect too has not been explored well in IR range.

4 Outlook

As indicated above, there are several possible extensions to the project. Phase transition temperature is a particularly important area to look at to further push up the tunability from 15%. Sub-wavelength tailoring of surface phonon polaritons, and in turn heat flux, can be a new starting point for exploring new control mechanisms of heat transfer using ferroelectric materials. Since perovskite structures are rich of tunable properties, such as ferromagnetic, piezoelectric and pyroelectric, there are certainly more to explore using ferroelectric system.

Moving away from ferroelectrics, more tunable materials or mechanisms for tunable heat transfer can also be explored. Tunable materials of interest include, for example, ferromagnetic materials which has properties tunable by magnetic field, optically controlled semiconductor

materials in which free carriers are excited within a thin layer close to the surface and many more.

Appendix A

Dyadic Green's Function: Free Space as an example

In many cases, finding Green's function is not trivial. Table A.1 is a list of Green's functions for some common operators [43]

Differential Operator $\hat{L}$	Green's Function G	Example of application
$\nabla^2=\partial x^2+\partial y^2$	$\frac{1}{2\pi}ln\varrho$	
$\nabla^2=\partial x^2+\partial y^2+\partial z^2$	$\frac{-1}{4\pi r}$	Poisson equation
Helmholtz operator ∇^2+k^2	$\frac{-e^{-ikr}}{4\pi r}$	Stationary Schrodinger equation
D'Alembert operator $\frac{1}{c^2}\partial t^2-\nabla^2$	$\frac{\delta(t-r/c)}{4\pi r}$	Wave equation

Table A.1: Green's function for different linear operators L (need to fix table)

Eigenfunction expansion is a widely used method for finding Green's function for Inhomogeneous Helmholtz Equation (IHE). The first step is to first find basis of the corresponding Homogenous Helmholtz Equation (HHE) (no perturbation or $\vec{J}=0$). The Green's function is then expressed as a linear sum of all basis function, and each coefficient for the basis functions is found using Fourier transform.

In the following paragraphs, IHE for stationary Schrödinger equation will be solved. The time-independent Schrödinger equation can be simplified as IHE (why S. Equation, not Maxwell Eq.)

$$-\frac{\hbar^2}{2m}\nabla^2\psi(\vec{r})+V(\vec{r})\psi(\vec{r})=E\psi(\vec{r})$$

$$\nabla^2\psi(\vec{r})+k^2\psi(\vec{r})=\frac{2m}{\hbar^2}V(\vec{r})\psi(\vec{r})$$

$$k^2=\frac{2mE}{\hbar^2}$$

where $V(r)$ is the scattering potential. The asymptotic form of the solution can be assumed as

$$\psi(\vec{r})\sim e^{i\vec{k_0}\cdot\vec{r}}+f_k(\theta,\phi)\frac{e^{ikr}}{r}=e^{i\vec{k_0}\cdot\vec{r}}+\Phi(\vec{r}) \qquad (A.1)$$

where the first term is the incident plane wave with wave vector $\vec{k}_0$, and the second term is the outgoing spherical wave with angular dependent amplitude factor f_k. Plugging in the solution to stationary Schf'odinger equation, terms related to incident plane wave cancel out, and the equation is left with

$$(\nabla^2 + k_0^2)\Phi(\vec{r}) = U(\vec{r})e^{ik_0 z} + U(\vec{r})\Phi(\vec{r}) \tag{A.2}$$

where $\frac{\hbar^2}{2m}U(\vec{r}) = V(\vec{r})$. The second term on the right $U(\vec{r})\Phi(\vec{r})$ can be neglected due to small probability of scattering. Final form of the simplification is a IHE [43],

$$(\nabla^2 + k_0^2)\Phi(\vec{r}) = U(\vec{r})e^{ik_0 z} \tag{A.3}$$

Step 1: Find a orthonormal set of eigenfunctions

The orthonormal set doesn't have to be unique. Depending on the geometry, it can be spherical waves, plane waves or other forms. In this case, plane wave is chosen, which are solutions of $(\nabla^2 + k^2)\psi_{\vec{k}}(\vec{r}) = 0$.

The equations are of form $\psi_{\vec{k}}(\vec{r}) = (2\pi)^{-3/2}e^{i\vec{k}\cdot\vec{r}}$. They also form an orthonormal set in position-space, or r-space.

$$\int \psi^*_{\vec{k}_1}(\vec{r})\psi_{\vec{k}_2}(\vec{r})d^3r = \delta(\vec{k}_1 - \vec{k}_2) \tag{A.4}$$

Step 2: Expand unknown function in eigenfunctions

The unknown function $\Phi(\vec{r})$ is expressed in terms of the eigenfunctions ψ_{k_1} as a Fourier integral,

$$\Phi(\vec{r_1}) = \int A_{\vec{k}_1}\psi_{\vec{k}_1}(\vec{r}_1)d^3k_1 \tag{A.5}$$

Substituting Equation A.5 into Equation A. 3,

$$\int A_{\vec{k_1}}(k_0^2 - k_1^2)\psi_{\vec{k}_1}(\vec{r})d^3k_1 = U(\vec{r})e^{ik_0 z} \tag{A.6}$$

where A_k are treated as constants and don't depend on position r.

Step 3: Find unknown coefficients using Fourier integral

Multiplying both sides by $\psi^*_{\vec{k}_2}(\vec{r})$ and integrate over the r-coordinates, or space coordinates,

$$\begin{aligned}\int A_{\vec{k_1}}(k_0^2 - k_1^2)d^3k_1 \int \psi^*_{\vec{k}_2}(\vec{r})\psi_{\vec{k}_1}(\vec{r})d^3r &= \int A_{\vec{k_1}}(k_0^2 - k_1^2)\delta(\vec{k}_1 - \vec{k}_2)d^3k_1 \\ &= A_{\vec{k_2}}(k_0^2 - k_2^2) \\ &= \int \psi^*_{\vec{k}_2}(\vec{r})U(\vec{r})e^{ik_0 z}d^3r\end{aligned}$$

Coefficients $A_{\vec{k}_2}$ are solved and substituted back into the original expansion to get

$$A_{\vec{k}_2} = (k_0^2 - k_2^2)^{-1} \int \psi^*_{\vec{k}_2}(\vec{r}) U(\vec{r}) e^{ik_0 z} d^3 r$$

$$\Phi(\vec{r_2}) = \int \left[(k_0^2 - k_2^2)^{-1} \int \psi^*_{\vec{k}_2}(\vec{r}_1) U(\vec{r}_1) e^{ik_0 z_1} d^3 r_1 \right] \psi_{\vec{k}_2}(\vec{r}_2) d^3 k_2$$

$$\Phi(\vec{r_1}) = \int (k_0^2 - k_1^2)^{-1} \psi_{\vec{k}_1}(\vec{r}_1) d^3 k_1 \int \psi^*_{\vec{k}_1}(\vec{r}_2) U(\vec{r}_2) e^{ik_0 z_2} d^3 r_2$$

Step 4: Find explicit forms of Green's function using contour integration

The results above can be written as a convolution between Green's function and the perturbation $U(\vec{r}_2)e^{ik_0 z_2}$, then the Green's function is defined as

$$G_{k_0}(\vec{r}_1, \vec{r}_2) = \int \frac{\psi^*_{\vec{k}_1}(\vec{r}_2)\psi_{\vec{k}_1}(\vec{r}_1)}{k_1^2 - k_0^2} d^3 k_1 \tag{A.7}$$

The Green's function can be solved explicitly assuming $\phi_{\vec{k}}(\vec{r})$ are plane wave solutions. Since solutions are polar symmetric, the integral can be written as

$$G_{k_0}(\vec{r}_1, \vec{r}_2) = \frac{1}{(2\pi)^3} \int_0^{+\infty} \int_0^{\pi} \int_0^{2\pi} \frac{e^{ik\rho cos\theta}}{k^2 - k_0^2} d\psi sin\theta d\theta k^2 dk. \tag{A.8}$$

Here since $\vec{r}_1 - \vec{r}_2$ is fixed for each Green's function, assume it as the polar coordinate $\vec{r}$ in k-space. Thus $\vec{k} \cdot (\vec{r}_1 - \vec{r}_2) = k\rho cos\theta$. The solution can be integrated using polar coordinates:

$$G_{k_0}(\vec{r}_1, \vec{r}_2) = \frac{1}{4\pi^2 \rho i} \int_0^{+\infty} \frac{e^{ik\rho} - e^{-ik\rho}}{k^2 - k_0^2} k dk$$

$$G_{k_0}(\vec{r}_1, \vec{r}_2) = \frac{1}{8\pi^2 \rho i} \int_{-\infty}^{+\infty} \frac{e^{i\kappa} - e^{-i\kappa}}{\kappa^2 - \sigma^2} \kappa d\kappa \tag{A.9}$$

Here $\kappa = k\varrho$ and $\sigma = k_0\varrho$. The last step involves contour integration in complex analysis. This is because the integral goes to infinity as the denominator goes to zero. The singular point can be avoided by contour integral.

$$G_{k_0}(\vec{r}_1, \vec{r}_2) = \frac{1}{8\pi^2 \rho i} \oint_C 1 \frac{e^{i\kappa}}{\kappa^2 - \sigma^2} \kappa d\kappa + \frac{1}{8\pi^2 \rho i} \oint_C 2 \frac{e^{-i\kappa}}{\kappa^2 - \sigma^2} \kappa d\kappa \tag{A.11}$$

$$G_{k_0}(\vec{r}_1, \vec{r}_2) = \frac{1}{8\pi^2 \rho i} (2\pi i \cdot \frac{1}{2} e^{i(\sigma + i\gamma)} + 2\pi i \cdot \frac{1}{2} e^{i(\sigma + i\gamma)}) \tag{A.12}$$

where the contour C_1 is a semicircle in upper half-plane, and C_2 is a semicircle in lower half-plane. The final expression for Green's function is simple

$$G_{k_0}(\vec{r}_1, \vec{r}_2) = \frac{1}{4\pi\rho} e^{i\sigma} \tag{A.13}$$

Green's functions for Laplacian operator and Poisson equations in different dimensions can be found in the same way[43].

References

[1]Planck, M. (1905). The Theory of Heat Radiation. *molecules*, *6*, 1023.

[2]Shen, S., Narayanaswamy, A., & Chen, G. (2009). Surface phonon polaritons mediated energy transfer between nanoscale gaps. *Nano Letters*, *9*(8), 2909-2913.

[3]Costescu, R. M., Wall, M. A., & Cahill, D. G. (2003). Thermal conductance of epitaxial interfaces. *Physical Review B*, *67*(5), 054302.

[4]Polder, D., & Van Hove, M. (1971). Theory of radiative heat transfer between closely spaced bodies. *Physical Review B*, *4*(10), 3303.

[5]Rytov, S. M. (1959). *Theory of electric fluctuations and thermal radiation* (No. AFCRC-TR-59-162). AIR FORCE CAMBRIDGE RESEARCH LABS HANSCOM AFB MA.

[6]Narayanaswamy, A., Shen, S., Hu, L., Chen, X., & Chen, G. (2009). Breakdown of the Planck blackbody radiation law at nanoscale gaps. *Applied Physics A*, *96*(2), 357-362.

[7]Domoto, G. A., Boehm, R. F., & Tien, C. L. (1970). Experimental investigation of radiative transfer between metallic surfaces at cryogenic temperatures.*Journal of Heat Transfer*, *92*(3), 412-416.

[8]Hargreaves, C. M. (1969). Anomalous radiative transfer between closely-spaced bodies. *Physics Letters A*, *30*(9), 491-492.

[9]Xu, J. B., Läuger, K., Möller, R., Dransfeld, K., & Wilson, I. H. (1994). Heat transfer between two metallic surfaces at small distances. *Journal of Applied Physics*, *76*(11), 7209-7216.

[10]Yugami, H., Sai, H., Nakamura, K., Nakagawa, N., & Ohtsubo, H. (2000). Solar thermophotovoltaic using $Al_2O_3/Er_3Al_5O_{12}$ eutectic composite selective emitter. In *Photovoltaic Specialists Conference, 2000. Conference Record of the Twenty-Eighth IEEE* (pp. 1214-1217). IEEE.

[11]DiMatteo, R. S., Greiff, P., Finberg, S. L., Young-Waithe, K. A., Choy, H. K. H., Masaki, M. M., & Fonstad, C. G. (2001). Enhanced photogeneration of carriers in a semiconductor via coupling across a nonisothermal nanoscale vacuum gap. *Applied Physics Letters*, *79*(12), 1894-1896.

[12]Lenert, A., Bierman, D. M., Nam, Y., Chan, W. R., Celanović, I., Soljačić, M., & Wang, E. N. (2014). A nanophotonic solar thermophotovoltaic device. *Nature nanotechnology*.

[13]Kolm, H. H. (1956). Solar-battery power source. *Quarterly Progress Report,13*.

[14]Yu, Z., Sergeant, N. P., Skauli, T., Zhang, G., Wang, H., & Fan, S. (2013). Enhancing far-field thermal emission with thermal extraction. *Nature Communications*, *4*, 1730.

[15] Greffet, J. J., Carminati, R., Joulain, K., Mulet, J. P., Mainguy, S., & Chen, Y. (2002). Coherent emission of light by thermal sources. *Nature*, *416*(6876), 61-64.

[16]Joulain, K., Carminati, R., Mulet, J. P., & Greffet, J. J. (2003). Definition and measurement of the local density of electromagnetic states close to an interface. *Physical Review B*, *68*(24), 245405.

[17]Narayanaswamy, A., & Chen, G. (2005). Direct computation of thermal emission from nanostructures. *Annual Review of Heat Transfer*, *14*(14).

[18]Narayanaswamy, A., & Chen, G. (2010). Dyadic Green's functions and electromagnetic local density of states. *Journal of Quantitative Spectroscopy and Radiative Transfer*, *111*(12), 1877-1884.

[19] Francoeur, M., Pinar Mengüç, M., & Vaillon, R. (2009). Solution of near-field thermal radiation in one-dimensional layered media using dyadic Green's functions and the scattering matrix method. *Journal of Quantitative Spectroscopy and Radiative Transfer*, *110*(18), 2002-2018.

[20] Chan, D. L., Soljačić, M., & Joannopoulos, J. D. (2006). Thermal emission and design in 2D-periodic metallic photonic crystal slabs. *Optics Express*, *14*(19), 8785-8796.

[21] Guo, Y., Cortes, C. L., Molesky, S., & Jacob, Z. (2012). Broadband super-Planckian thermal emission from hyperbolic metamaterials. *Applied Physics Letters*, *101*(13), 131106.

[22] Narayanaswamy, A., & Chen, G. (2003). Surface modes for near field thermophotovoltaics. *Applied Physics Letters*, *82*(20), 3544-3546.

[23] Liu, X., Tyler, T., Starr, T., Starr, A. F., Jokerst, N. M., & Padilla, W. J. (2011). Taming the blackbody with infrared metamaterials as selective thermal emitters. *Physical Review Letters*, *107*(4), 045901.

[24] Messina, R., & Ben-Abdallah, P. (2013). Graphene-based photovoltaic cells for near-field thermal energy conversion. *Scientific Reports, 3.*

[25] S. V. Boriskina, H. Ghasemi, and G. Chen (2013), "Plasmonic materials for advanced energy applications." *Materials Today* 16(10), 375-386..

[26] Guha, B., Otey, C., Poitras, C. B., Fan, S., & Lipson, M. (2012). Near-Field radiative cooling of nanostructures. *Nano Letters, 12*(9), 4546-4550.

[27] Fu, C. J., & Zhang, Z. M. (2006). Nanoscale radiation heat transfer for silicon at different doping levels. *International Journal of Heat and Mass Transfer,49*(9), 1703-1718.

[28] Chen, F., Klimchitskaya, G. L., Mostepanenko, V. M., & Mohideen, U. (2007). Control of the Casimir force by the modification of dielectric properties with light. *Physical Review B, 76*(3), 035338.

[29] Dalvit, D. A., & Lamoreaux, S. K. (2008). Contribution of drifting carriers to the Casimir-Lifshitz and Casimir-Polder interactions with semiconductor materials. *Physical Review Letters, 101*(16), 163203.

[30] Basu, S., & Francoeur, M. (2011). Near-field radiative transfer based thermal rectification using doped silicon. *Applied Physics Letters, 98*(11), 113106.

[31] Van Zwol, P. J., Thiele, S., Berger, C., De Heer, W. A., & Chevrier, J. (2012). Nanoscale radiative heat flow due to surface plasmons in graphene and doped silicon. *Physical Review Letters, 109*(26), 264301.

[32] Shi, J., Li, P., Liu, B., & Shen, S. (2013). Tuning near field radiation by doped silicon. *Applied Physics Letters, 102*(18), 183114.

[33] Cui, L., Huang, Y., Wang, J., & Zhu, K. Y. (2013). Ultrafast modulation of near-field heat transfer with tunable metamaterials. *Applied Physics Letters, 102*(5), 053106.

[34] Ilic, O., Jablan, M., Joannopoulos, J. D., Celanovic, I., Buljan, H., & Soljačić, M. (2012). Near-field thermal radiation transfer controlled by plasmons in graphene. *Physical Review B, 85*(15), 155422.

[35] Ben-Abdallah, P., & Biehs, S. A. (2014). Near-field thermal transistor. *Physical Review Letters, 112*(4), 044301.

[36] Nyquist, H. (1928). Thermal agitation of electric charge in conductors. *Physical Review*, *32*(1), 110-113.

[37] Callen, H. B., & Welton, T. A. (1951). Irreversibility and generalized noise.*Physical Review*, *83*(1), 34-40.

[38] Joulain, K., Mulet, J. P., Marquier, F., Carminati, R., & Greffet, J. J. (2005). Surface electromagnetic waves thermally excited: Radiative heat transfer, coherence properties and Casimir forces revisited in the near field. *Surface Science Reports*, *57*(3), 59-112.

[39] K. B. Tolpygo (2008). "Physical properties of a rock salt lattice made up of deformable ions," *Ukr. J. Phys.*, 53(Special Issue), 93-102

[40] Ashcroft, N. W., Mermin, N. D., & Rodriguez, S. (1978). Solid State Physics.

[41] Feurer, T., Stoyanov, N. S., Ward, D. W., Vaughan, J. C., Statz, E. R., & Nelson, K. A. (2007). Terahertz polaritonics. *Annu. Rev. Mater. Res.*, *37*, 317-350.

[42] Maier, S. A. (2007). *Plasmonics: Fundamentals and Applications: Fundamentals and Applications*. Springer.

[43] Arfken, G. B., Weber, H. J., & Spector, D. (1999). Mathematical methods for physicists.

[44] Appel, W. (2001). *Mathematics for Physics and Physicists*. Princeton University Press.

[45] J. A. Kong, "Green's functions for planarly layered media." http://ocw.mit.edu/courses/electrical-engineering-and-computer-science/6-635-advanced-electromagnetism-spring-2003/lecture-notes/, 2003.

[46] L. Novotny and B. Hecht (2012). *Principles of Nano-Optics*. Cambridge University Press.

[47] Chen, D. Z., & Chen, G. (2010). Heat flow in thin films via surface phonon-polaritons. *Frontiers in Heat and Mass Transfer (FHMT)*, *1*(2).

[48] C. Kittel (1996). *Introduction to Solid State Physics*. Wiley.

[49] Haeni, J. H., Irvin, P., Chang, W., Uecker, R., Reiche, P., Li, Y. L., and Schlom, D. G. (2004). Room-temperature ferroelectricity in strained SrTiO3. *Nature*, *430*(7001), 758-761.

[50] "Titchmarsh theorem." http://mathworld.wolfram.com/TitchmarshTheorem.html. (Last retrieved: May 15, 14)

[51] "Causality and analyticity." http://rickbradford.co.uk/ChoiceCutsCh34.pdf. (Last retrieved: May 15, 14)

[52] "Ferroelectric structure during phase change." http://www.doitpoms.ac.uk/tlplib/ferroelectrics/printall.php. (Last retrieved: May 15, 14)

[53] Stirling, W. G. (1972). Neutron inelastic scattering study of the lattice dynamics of strontium titanate: harmonic models. *Journal of Physics C: Solid State Physics*, *5*(19), 2711.

[54] Fleury, P. A., Scott, J. F., & Worlock, J. M. (1968). Soft Phonon Modes and the 110° K Phase Transition in SrTiO3. *Physical Review Letters*, *21*(1), 16.

[55] Fleury, P. A., & Worlock, J. M. (1968). Electric-Field-Induced Raman Scattering in SrTiO3 and KTaO3. *Physical Review*, *174*(2), 613.

[56] Kadlec, C., Skoromets, V., Kadlec, F., Němec, H., Hlinka, J., Schubert, J., ... & Kužel, P. (2009). Temperature and electric field tuning of the ferroelectric soft mode in a strained SrTiO 3/DyScO3 heterostructure. *Physical Review B*,*80*(17), 174116.

[57] Pelaiz-Berranco, A. and Guerra, J. D. S. (2010). Dielectric Relaxation Phenomenon in Ferroelectric Pervoskite-related Structures. http://cdn.intechopen.com/pdfs-wm/12496.pdf. (Last retrieved: May 15, 14)

[58] Skoromets, V., Kadlec, C., Kuzel, P., Kamba, S., & Schubert, J. (2010). Electric field tuning of hard polar phonons in strained SrTiO3 films. *Journal of Applied Physics*, *107*(12), 124116-124116.

[59] Cheng, Z. Y., Katiyar, R. S., Yao, X., & Bhalla, A. S. (1998). Temperature dependence of the dielectric constant of relaxor ferroelectrics. *Physical Review B*, *57*(14), 8166.

[60] Kristoffel, N., & Konsin, P. (1973). Electron-phonon interaction, microscopic mechanism and properties of ferroelectric phase transitions. *Ferroelectrics*,*6*(1), 3-12.

[61] Cowley, R. A. (1965). On the theory of ferroelectricity and anharmonic effects in crystals. *Philosophical Magazine*, *11*(112), 673-706.

[62] Cross, L. E. (1987). Relaxor ferroelectrics. *Ferroelectrics*, *76*(1), 241-267.

[63] Cowley, R. A., Gvasaliya, S. N., Lushnikov, S. G., Roessli, B., & Rotaru, G. M. (2011). Relaxing with relaxors: a review of relaxor ferroelectrics. *Advances in Physics*, *60*(2), 229-327.

[64] Antons, A., Neaton, J. B., Rabe, K. M., & Vanderbilt, D. (2005). Tunability of the dielectric response of epitaxially strained SrTi O 3 from first principles. *Physical Review B*, *71*(2), 024102.

[65] Wang, X., & Vanderbilt, D. (2007). First-principles perturbative computation of dielectric and Born charge tensors in finite electric fields. *Physical Review B*,*75*(11), 115116.

[66] Francoeur, M., Mengüç, M. P., & Vaillon, R. (2010). Spectral tuning of near-field radiative heat flux between two thin silicon carbide films. *Journal of Physics D: Applied Physics*, *43*(7), 075501.

[67] Ocelic, N., & Hillenbrand, R. (2004). Subwavelength-scale tailoring of surface phonon polaritons by focused ion-beam implantation. *Nature Materials*, *3*(9), 606-609.

[68] Wu, Y., Forbess, M. J., Seraji, S., Limmer, S. J., Chou, T. P., & Cao, G. (2001). Oxygen-vacancy-related dielectric relaxation in SrBi2Ta1. 8V0. 2O9 ferroelectrics. *Journal of Applied Physics*, *89*(10), 5647-5652.

[69] Park, S. J., Lee, J. P., Jang, J. S., Rhu, H., Yu, H., You, B. Y., ... and Lee, W. (2013). In situ control of oxygen vacancies in TiO2 by atomic layer deposition for resistive switching devices. *Nanotechnology*, *24*(29), 295202.

[70] Gurk, P. (1972). Contribution of domain wall motion to the permittivity of Rochelle salt. *Physica Status Solidi (a)*, *10*(2), 407-414.

[71] Xu, R., Karthik, J., Damodaran, A. R., & Martin, L. W. (2014). Stationary domain wall contribution to enhanced ferroelectric susceptibility. *Nature Communications*, *5*.

[72] Hafeli, A. K., Rephaeli, E., Fan, S., Cahill, D. G., & Tiwald, T. E. (2011). Temperature dependence of surface phonon polaritons from a quartz grating. *Journal of Applied Physics*, *110*(4), 043517.